IRAQI JOURNAL OF APPLIED PHYSICS

The *Iraqi Journal of Applied Physics (IJAP)* is a peer reviewed journal of high quality devoted to the publication of original research papers from applied physics and their broad range of applications. IJAP publishes quality original research papers, comprehensive review articles, survey articles, book reviews, dissertation abstracts in physics and its applications in the broadest sense. It is intended that the journal may act as an interdisciplinary forum for Physics and its applications. Innovative applications and material that brings together diverse areas of Physics are particularly welcome. Review articles in selected areas are published from time to time. It aims to disseminate knowledge; provide a learned reference in the field; and establish channels of communication between academic and research experts, policy makers and executives in industry, commerce and investment institutions. IJAP is a quarterly specialized periodical dedicated to publishing original papers, letters and reviews in: Applied & Nonlinear Optics, Applied Mechanics & Thermodynamics, Digital & Optical Communications, Electronic Materials & Devices, Laser Physics & Applications, Plasma Physics & Applications, Quantum Physics & Spectroscopy, Semiconductors & Optoelectronics, Solid State Physics & Applications, Alternative and Renewable Energy, and Computers and Networks.

ISSN (Print): 1813-2065, ISSN (Online): 2309-1673, ISSN (Letters): 1999-656X

EDITORIAL BOARD

Raad A. KHAMIS	Asst. Professor	Editor-in-Chief	Plasma Physics	IRAQ
Walid K. HAMOUDI	Professor	Member	Laser Physics	IRAQ
Dayah N. RAOUF	Asst. Professor	Member	Laser and Optics	IRAQ
Raid A. ISMAIL	Professor	Member	Semiconductor Physics	IRAQ
Oday A. HAMMADI	Asst. Professor	Managing Editor	Molecular Physics	IRAQ
Intesar F. RAMLEY	Professor	Member	Communications Eng.	CANADA
Khaled A. AHMED	Professor	Member	Theoretical Physics	IRAQ
Manal J. AL-KINDY	Asst. Professor	Member	Electrical Engineering	IRAQ
Kais A. AL-NAIMEE	Asst. Professor	Member	Quantum Optics	ITALY
Abdulhadi ALKHALILI	Professor	Member	Medical Physics	U.S.A
Abdulmajeed IBRAHIM	Professor	Member	Solid State Physics	IRAQ
Loay E. GEORGE	Asst. Professor	Member	Computers & Networks	IRAQ
Haitham M. MIKHLIF	Lecturer	Member	Molecular Physics	UK

Editorial Office:
P. O. Box 55259, Baghdad 12001, IRAQ
Website: www.iraqiphysicsjournal.com
Emails: info@iraqiphysicsjournal.com, editor_ijap@yahoo.co.uk, editor@ijaponline.com

ADVISORY BOARD

Abdullah M. SUHAIL, Professor, Department of Physics, College of Science, University of Baghdad, IRAQ
Adel K. HAMOUDI, Professor, Department of Physics, College of Science, University of Baghdad, IRAQ
Andrei KASIMOV, Professor, Institute of Material Science, National Academy of Science of Ukraine, Kiev, UKRAINE
Ashok KUMAR, Professor, Harcourt Butler Technological Institute, Nawabganj, Kanpur, Uttar Pradesh 208 002, INDIA
Chang Hee NAM, Professor, Korean Advanced Institute of Science and Technology, 291 Daehak-ro, Daejeon, KOREA
El-Sayed M. FARAG, Professor, Department of Sciences, College of Engineering, Al-Minofiya University, EGYPT
Franko KUEPPERS, Professor, Darmstadt University of Technology, Mornewegstraße 32, Darmstadt, GERMANY
Gang XU, Assistant Professor, Department of Engineering and Physics, University of Central Oklahoma, U.S.A
Heidi ABRAHAMSE, Professor, Faculty of Health Sciences, University of Johannesburg, SOUTH AFRICA
Mansoor SHEIK-BAHAE, Associate Professor, Department of Physics & Astronomy, University of New Mexico, U.S.A
Mazin M. ELIAS, Professor, Laser Institute for Postgraduates, University of Baghdad, Al-Jadiriyah, Baghdad, IRAQ
Mohammad Robi HOSSAN, Assistant Professor, Dept. of Engineering and Physics, Univ. of Central Oklahoma, U.S.A
Mohammed A. HABEEB, Professor, Department of Physics, Faculty of Science, Al-Nahrain University, Baghdad, IRAQ
Morshed KHANDAKER, Associate Professor, Dept. of Engineering and Physics, Univ. of Central Oklahoma, U.S.A
Muhammad A. HUSSAIN, Assistant Professor, Dept. of Laser and Optoelectronics Eng., Al-Nahrain University, IRAQ
Mutaz S. ABDUL-WAHAB, Assistant Professor, Dept. of Electric and Electronic Eng., University of Technology, IRAQ
Nadir F. HABOUBI, Professor, Department of Physics, College of Education, Al-Mustansiriya Univ., Baghdad, IRAQ
Shivaji H. PAWAR, Professor, D.Y. Patil University, Kasaba Bawada, Kolhapur-416 006, INDIA
Xueming LIU, Professor, Department of Electronic Engineering, Tsinghua University, Shuang Qing Lu, Beijing, CHINA
Yanko SAROV, Assistant Professor, Micro- and Nanoelectronic Systems, Technical University Ilmenau, GERMANY
Yushihiro TAGUCHI, Professor, Department of Physics, Chuo University, Higashinakano Hachioji-shi, Tokyo, JAPAN

SPONSORED AND PUBLISHED BY
THE IRAQI SOCIETY FOR ALTERNATIVE AND RENEWABLE ENERGY SOURCES & TECHNIQUES (I.S.A.R.E.S.T.)

IRAQI JOURNAL OF APPLIED PHYSICS

ISSN (Print): 1813-2065, ISSN (Online): 2309-1673, ISSN (Letters): 1999-656X

" INSTRUCTIONS TO AUTHORS "

CONTRIBUTIONS

Contributions to be published in this journal should be original research works, i.e., those not already published or submitted for publication elsewhere, individual papers or letters to editor.
Manuscripts should be submitted to the editor at the mailing address:

Iraqi Journal of Applied Physics, Editorial Board, P. O. Box 55259, Baghdad 12001, IRAQ
Website: www.iraqiphysicsjournal.com
Email: editor@iraqiphysicsjournal.com, editor_ijap@yahoo.co.uk

MANUSCRIPTS

Two hard copies with soft copy on a compact disc (CD) should be submitted to Editor in the following configuration:

- **One-column** Double-spaced one-side A4 size with 2.5 cm margins of all sides
- Times New Roman font (16pt bold for title, 14pt bold for names, 12pt bold for headings, 12pt regular for text)
- Letters should not exceed 10 pages, papers should not exceed 20 pages and reviews are up to author.
- Manuscripts presented in English only are accepted.
- English abstract not exceed 150 words
- 4 keywords (at least) should be maintained on (PACS preferred)
- Author(s) should express all quantities in SI units
- Equations should be written in equation form (*italic* and symbolic)
- Figures and Tables should be separated from text
- Figures and diagrams can be submitted in colors for assessment and they will be returned to authors after provide printable copies
- Charts should be indicated by the software used for
- Only original or high-resolution scanner photos are accepted
- For electronic submission, articles should be formatted with MS-Word software.

AUTHOR NAMES AND AFFILIATIONS

It is IJAP policy that all those who have participated significantly in the technical aspects of a paper be recognized as co-authors or cited in the acknowledgments. In the case of a paper with more than one author, correspondence concerning the paper will be sent to the first author unless staff is advised otherwise.
Author name should consist of first name, middle initial, last name. The author affiliation should consist of the following, as applicable, in the order noted:
- Company or college (with department name or company division), Postal address, City, state, zip code, Country name, contacting telephone, and e-mail

REFERENCES

The references should be brought at the end of the article, and numbered in the order of their appearance in the paper. The reference list should be cited in accordance with the following examples:

[1] X. Ning and M.R. Lovell, "On the Sliding Friction Characteristics of Unidirectional Continuous FRP Composites", *ASME J. Tribol.*, 124(1) (2002) 5-13.
[2] M. Barnes, "Stresses in Solenoids", *J. Appl. Phys.*, 48(5) (2001) 2000–2008.
[3] J. Jones, **"Contact Mechanics"**, Cambridge University Press (Cambridge, UK) (2000), Ch.6, p.56.
[4] Y. Lee, S.A. Korpela and R. Horne, "Structure of Multi-Cellular Natural Convection in a Tall Vertical Annulus", Proc. 7th International Heat Transfer Conference, U. Grigul et al., eds., Hemisphere (Washington DC), 2 (1982) 221–226.
[5] M. Hashish, "Waterjet Technology Development", High Pressure Technology, PVP-Vol. 406 (2000) 135-140.
[6] D.W. Watson, "Thermodynamic Analysis", ASME Paper No. 97-GT-288 (1997).
[7] C.Y. Tung, "Evaporative Heat Transfer in the Contact Line of a Mixture", Ph.D. thesis, Rensselaer Polytechnic Institute, Troy, NY (1982).

PROOFS

Authors will receive proofs of papers and are requested to return one corrected hard copy with a WORD copy on a compact disc (CD). New materials inserted in the original text without Editor permission may cause rejection of paper.

COPYRIGHT FORM

Author(s) will be asked to transfer copyrights of the article to the Journal soon after acceptance of it. This will ensure the widest possible dissemination of information.

OFFPRINTS

Authors will receive offprints free of charge and any additional reprints can be ordered.

SUBSCRIPTION AND ORDERS

Annual fees (4 issues per year) of subscription are:

50 US$ for individuals inside Iraq;	**200** US$ for institutions inside Iraq;
100 US$ for individuals abroad;	**300** US$ for institutions abroad.

Fees are reduced by 25% for I.S.A.R.E.S.T. members. Orders of issues can be submitted by contacting the editor-in-chief or editorial office at admin@iraqiphysicsjournal.com, or editor_ijap@yahoo.co.uk to maintain the address of issue delivery and payment way.

IRAQI JOURNAL OF APPLIED PHYSICS
Vol. 16, No.3, July-September 2020, pp. 3-12

Effects of Rare Earth Dopants on Spectroscopic Properties of Silica Glasses Prepared by Sol-Gel Technique

Firas J. Kadhim

Department of Physics,
College of Science,
University of Baghdad,
Baghdad, IRAQ

In this work, the effects of doping of silica glasses with rare earth element on their spectroscopic properties were studied. The silica glass monoliths were prepared by sol-gel technique and the doping process was carried out using different molar concentrations of aluminum and rare earth element (erbium). Results showed that the positions of the absorption bands in sol and bulk phases are similar to that of RE solutions, indicating the presence of RE^{3+} ions and its spectroscopic activity within the sample structure. It has also been noted that the present absorption spectra show inhomogeneous broadening which may be attributed to the amorphous character of sol-gel glass host.

Keywords: Silica glasses; Sol-gel; Rare earth dopants; Spectroscopy
Received:14 May 2020; **Revised:** 21 July 2020; **Accepted:** 28 July 2020

1. Introduction

Sol-gel glasses are nano-porous silica glass monoliths made by the sol-gel process. It features a narrow pore size distribution, a high degree of pore connectivity, and can hold a higher concentration of dopants than traditional melt glasses without losing their amorphous character [1-3]. Zachariasen's rules, which explained the structure of oxide glasses, are also applicable generally to sol-gel oxide glasses. The solid line in Fig. (1) represents melting, quenching, and reheating of silica oxide. The high temperature of melting point is clear, and during quenching, the undercooled liquid must pass through a temperature range. The solidified glass has no pores [4]. The dashed line represents the processing of gel-derived silica glass. Low-temperature reactions is clear and results in a porous amorphous solid. No melting has occurred, but the process required a longer time compared with melt glass [5].

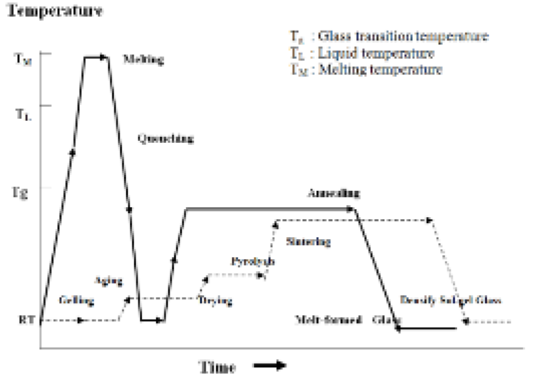

Fig. (1) Comparison of the processing steps of melt-derived glasses and sol-gel-derived glasses [5]

Rare earths (RE) ions are commonly used as dopants for the active media of solid-state lasers, because they seem to have abundance in fluorescence emission lines that cover all ranges of visible and near-infrared regions of the electromagnetic spectrum. The outermost electrons of these ions formed an integrable shell like Xenon shell, involving the filled 5s and 5d shells that shield the optically active 4f electrons [6-9].

2. Experimental Part

Glass monoliths of rod shape were prepared using the sol-gel technique. For each concentration of RE and Al ions, the final sol-gel solution was prepared in a convenient quantity and was poured in several glass tubes of 1.5 cm in diameter and 5 cm in length in order to perform different tests. The described procedure allowed us to produce glass rod samples with good transparency of diameter of 0.38-0.4 cm, measured by micrometer, length of 1.2-1.5 cm and weight of 0.1915-0.3837 gm. Figure (2) illustrates some of the final prepared samples.

Depending on the results of studying the effect of Al co-doping that would be discussed later, all measurements were achieved for the doped samples at molar concentration ratio Al:RE of 10 which gives the best spectroscopic properties.

Table (1) shows the primary percentage of RE^{3+} and Al^{3+} ions doped sol-gel glass samples obtained after sintering process, and the percentage measured by atomic absorption analysis. The results of this analysis show a good agreement in the percentage of the primary and measured values, indicating the efficiency and accuracy of the sol-gel method, and the proper heat treatment. The RE ion density was determined in both cases and the true volume of samples was measured by gas displacement method.

Fig. (2) Some of the prepared sol-gel glass rod samples doped with RE^{3+} and Al co-doping

Density of the prepared samples is determined depending on the true volume measured by the gas displacement method and the accurate weight as shown in table (2). The results show that the density of dense silica Xerogel obtained by drying the wet gel for ~2 days at 90-110 °C is less than its value for the doped sol-gel glass samples which is sintered for 1 hour at 500 ºC. However, time and temperature of the treated thermal process determine the true density of the silica gel optical material, which is supposed to increase with increasing these factors [10]. Also, because of the porosity of sol-gel silica structure, they have a low density compared with the theoretical density of the corresponding non-porous oxide. The structure of doped samples ultimately affects the RE^{3+} distribution in the materials, and thereby there is an increasing in the density of these samples as the RE^{3+} concentration increases. The same behavior is observed for all three types of RE ions, and may be attributed to the increasing of a relatively uniform distribution of these ions throughout the material. Our results show that the values of density for SHO5 and SEU5 glass rod samples are close to its value of non-porous silica glass, and this may be due to the increasing of the heavy RE ion distribution in the material pores especially at higher concentrations.

Hardness test indicates the deformation which happens on the surface of a material [11]. In order to test the surface homogeneities by Vickers hardness tester, the indentation was made in three regions; the two bases and the side of cylindrical rod area, for each sol-gel glass rod sample as shown in the flowing scheme:

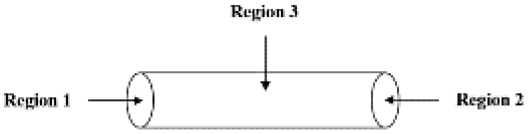

The impression diagonals for each sample were very similar as given in table (3), indicating that the chemical reaction of sol-gel process was completed and the suitable heat treatment (i.e. aging, drying and sintering) leads to obtain a silica sol-gel glass with high homogeneity. Vickers hardness values are determined depending on the applied load (F) and the contact area using the equation [11]:

$$HV= 2F\sin(68°)/d^2 \qquad (1)$$

where F= 0.98 N, $d^2/2\ \sin(136°/2)$ is the contact area and d is the impression diagonal. The results show that Vickers hardness values of silica sol-gel glasses are less than those of some melt-silica glass systems (see table 3). This means that the melt-silica glasses are harder and tougher than the silica sol-gel glasses, and can be attributed to the higher annealing temperatures of melt-silica glasses.

On the other hand, Vickers hardness values of doped samples are greater than that of pure sample, for example Vickers hardness of SER2 sample is (2.26 GPa) compared to (1.89 GPa) for pure sol-gel glass sample. This indicates that the dopants (i.e. RE and Al) may improve the mechanical stability of these glasses. However, some of previous researches remarked that one of the advantages of RE ions doped certain optical glasses is to give them a mechanical stability [12].

3. Results and Discussion

Figures (3) to (5) illustrate the absorption spectra of RE solutions and doped samples in sol and bulk phases at maximum concentration of RE^{3+} ions obtained in the present study.

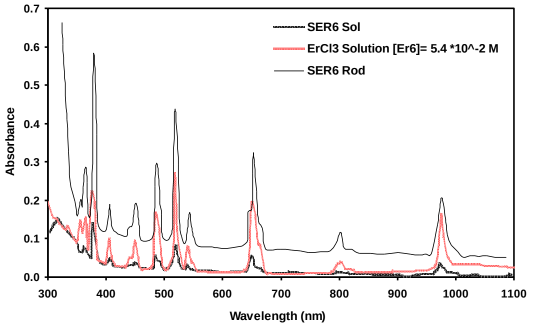

Fig. (3) The absorption spectra of Er^{3+} ion in three cases; Er - chloride solution, sol and bulk phases

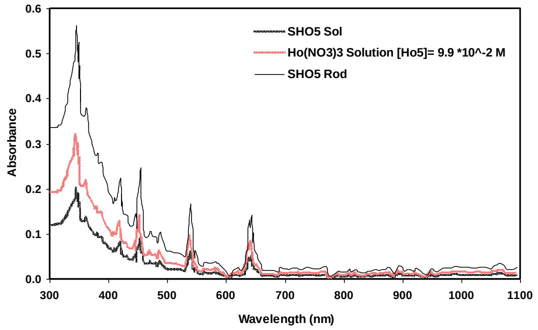

Fig. (4) The absorption spectra of Ho^{3+} ion in three cases; Ho-nitrate solution, sol and bulk phases

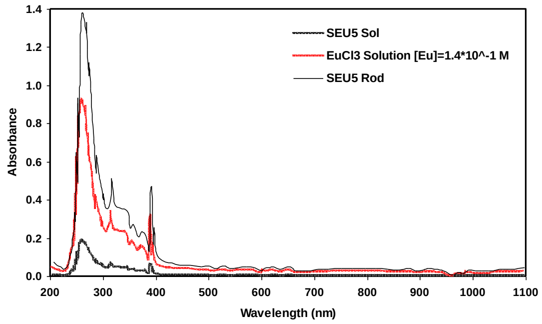

Fig. (5) The absorption spectra of Eu^{3+} ion in three cases; Eu-chloride solution, sol and bulk phases

Generally, the positions of the absorption bands in sol and bulk phases are similar to that of RE solutions, indicating the presence of RE^{3+} ions and its spectroscopic activity within the sample structure. It can be noticed from these figures that the absorbance at sol phase is too low because the concentration of RE^{3+} ions is diluted, while noticeable absorbance is achieved at bulk phase which is due to the effect of solvent evaporation that leads to concentrate the RE^{3+} ions in a smaller volume than that of sol volume. Also, the absorption bands in bulk phase have a little red shift in comparison with the RE solutions and sol phase. This may be explained as follows; when solid host is used, the RE^{3+} ions are located inside the pores of sol-gel glass structure [13]. So that there is an interaction between these ions as well as with its host environment and this may perturb its energy levels. Therefore the lowest 4f level may be shifted to lower energy. At low concentration, the RE^{3+} ions become more relaxed and at relatively large separation distance. These conditions will, therefore, reduce the perturbation processes and lead to decreasing this red shift more as observed in our results at lower RE^{3+} concentrations.

Figures (6) to (8) show the absorption coefficient vs. wavelength of bulk samples doped with different concentrations of RE^{3+} ions and at (Al: RE) of 10:1 molar concentration ratio. These spectra of our system are similar to other spectroscopic measurements of RE^{3+} ions doped other systems (melt-silica glasses and crystals) which are reported by other researches [14,15], as shown in the small in figures (6)-(8).

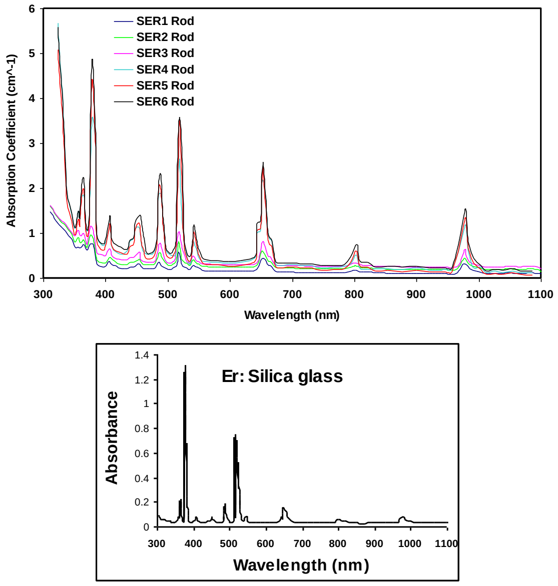

Fig. (6) The absorption spectra of Er^{3+} ion in SER Rod samples

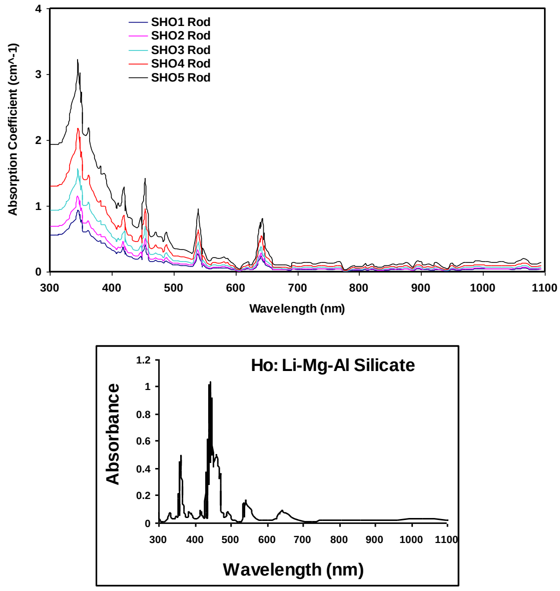

Fig. (7) The absorption spectra of Ho^{3+} ion in SHO Rod samples

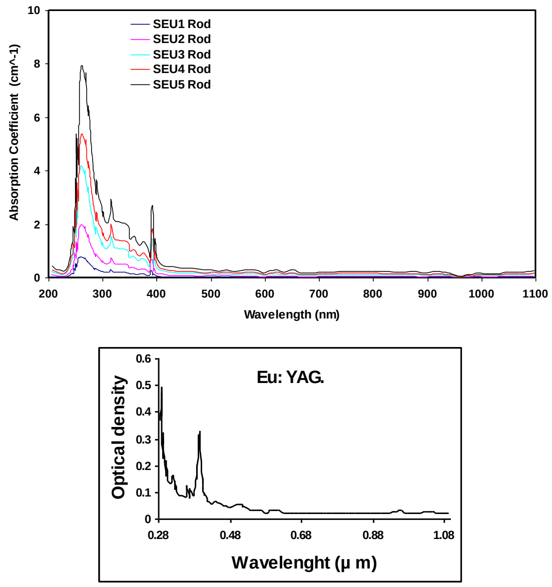

Fig. (8) The absorption spectra of Eu^{3+} ion in SEU Rod samples

The present results show that the absorption coefficient α (λ), at the peak of each band, is increased as a result of a corresponding increase of concentration. For example, the α (λ) is increased from 0.581 cm^{-1} to 3.593 cm^{-1} for the ($^4\boldsymbol{I}_{15/2}\rightarrow {}^2\boldsymbol{H}_{11/2}$, ~ 518 nm) transition of Er^{3+} ion (Fig. (6)), increased from 0.943 cm^{-1} to 3.24 cm^{-1} for the ($^5\boldsymbol{I}_8\rightarrow {}^5\boldsymbol{G}_2$, ~ 344 nm) transition of Ho^{3+} ion (Fig. (7)) and increased from 0.268 cm^{-1} to 2.69 cm^{-1} for the transition ($^7\boldsymbol{F}_0\rightarrow {}^5\boldsymbol{D}_3$, ~ 393 nm) of Eu^{3+} ion (Fig. (8)). This is due to that the probability of absorption process is increased as the RE^{3+} ions contribution in the glass host increases, according to Beers-Lambert law. Some of previous researches referred to that the increasing of α (λ) with the concentration leads to an increase in the pumping efficiency of glass host which used as laser media, and this can be positively reflected on the performance of these hosts [16].

It has been noted that the present absorption spectra show inhomogeneous broadening which may be attributed to the amorphous character of sol-gel glass host. In a glass host, every dopant will be surrounded by a slightly different electronic environment which affects the position of dopant energy levels slightly and the transition rate from one energy level to another slightly. The increasing of band width leads to an increased in the pumping efficiency of glass host by achieving the correspondence with the used pumping band [17].

The pure sol-gel glass sample demonstrates superior transmission to the doped samples tested in the same range as shown in Fig. (9). The flat transmission spectrum of pure sample is evidence that trace impurities and water are eliminated from the structure of sol-gel glass. This result suggests that the sol-gel glass may be closed to intrinsic vitreous silica. On the other hand, the transmittance of Er^{3+}-doped sol-gel glass samples decreased slightly as the Er^{3+} concentration increases. It may be induced by Er^{3+} ions only which result in absorbing more than scattering and reflecting and any band due to other impurities or water dose not exist. The same behavior is observed for Ho^{3+} and Eu^{3+} samples as shown in figures (10 and 11).

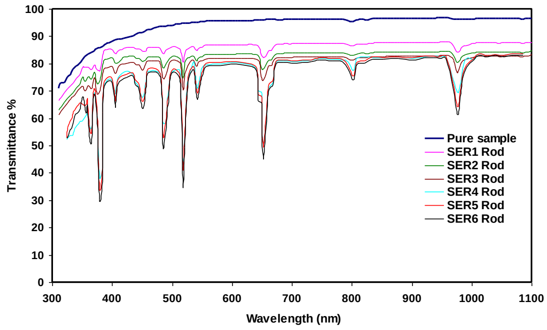

Fig. (9) UV-VIS-NIR Transmission of pure sol-gel glass (sample thickness 0.37 cm) and SER Rod samples (thickness of 0.39-0.4 cm)

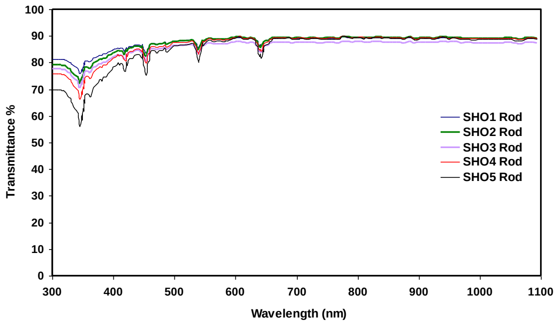

Fig. (10) UV-VIS-NIR Transmission of SHO Rod samples (thickness of 0.38-0.4 cm)

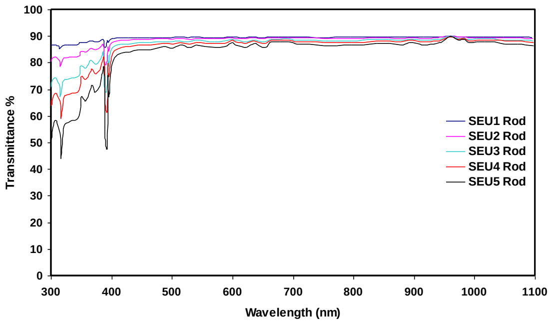

Fig. (11) UV-VIS-NIR Transmission of SEU Rod samples (thickness of 0.38-0.4 cm)

Figures (12) to (14) show the dispersion curves for sol-gel glass samples. The refractive index as a function of wavelength is obtained from the reflectance spectra measurements. It can be noted that, generally, the refractive index of all samples decreases with the increase of the wavelength, which is completely in agreement with the theory of refraction in glass systems [17]. While it increases with the increasing of RE^{3+} ions concentration, which is ascribed to two factors that contribute significantly to higher indices [18]. The first one is greater phase density. Secondly, the presence of atoms (RE^{3+} ions in our system) with higher atomic numbers, considering that the index of refraction is depends on the electronic polarizability of material which responds rapidly to interact at the frequency of visible light. This factor also explains the higher indices of Er^{3+} samples, which extended between (1.5-1.479) at visible region, comparing with (1.497-1.466) and (1.484-1.45) for Ho^{3+} and Eu^{3+} samples respectively. The dispersion curves of Er^{3+} and Ho^{3+} samples involved some of bands which corresponds the absorption bands that appears in the visible range. However, the limited change in index of refraction values of each sample indicates the good homogeneity of sol-gel glass samples.

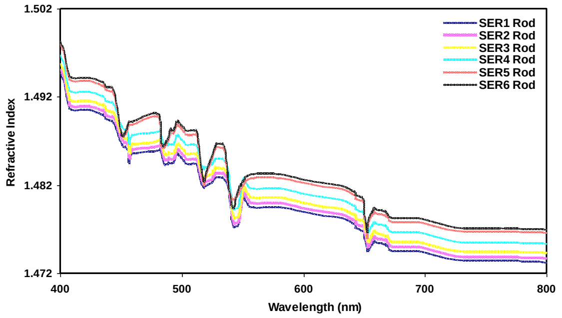

Fig. (12): Dispersion curves of Er^{3+}-doped sol-gel glass samples with Al co-doping

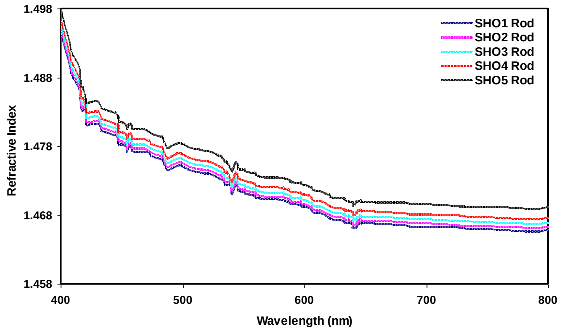

Fig. (13) Dispersion curves of Ho^{3+}-doped sol-gel glass samples with Al co-doping

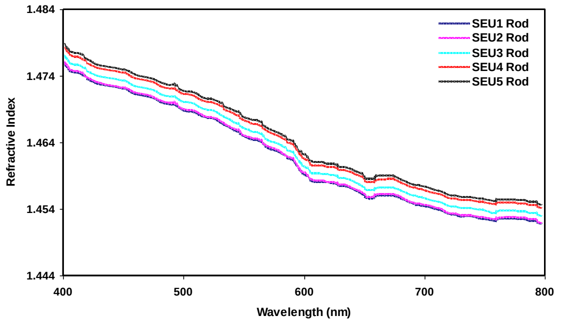

Fig. (14) Dispersion curves of Eu^{3+}-doped sol-gel glass samples with Al co-doping

The fluorescence spectra for different concentrations of Er^{3+}, Ho^{3+} and Eu^{3+} doped sol-gel glass samples with Al: RE molar ratio of 10:1 are illustrated in Fig. (15). Fluorescence measurements for Er^{3+} samples are performed using the 515 nm line of an Argon ion laser which corresponds to the peak of the absorption band due to the $^4\boldsymbol{I}_{15/2}\rightarrow {}^2\boldsymbol{H}_{11/2}$ transition of Er^{3+} ions. While the excitation wavelengths are: 344 nm for Ho^{3+} samples and 393 nm for Eu^{3+} samples, which are obtained by selection the output of a continuous Xenon lamp, that correspond to the peak of the absorption bands due to the $^5\boldsymbol{I}_8\rightarrow {}^5\boldsymbol{G}_2$ and $^7\boldsymbol{F}_0\rightarrow {}^5\boldsymbol{D}_3$ transitions of Ho^{3+} and Eu^{3+} ions, respectively.

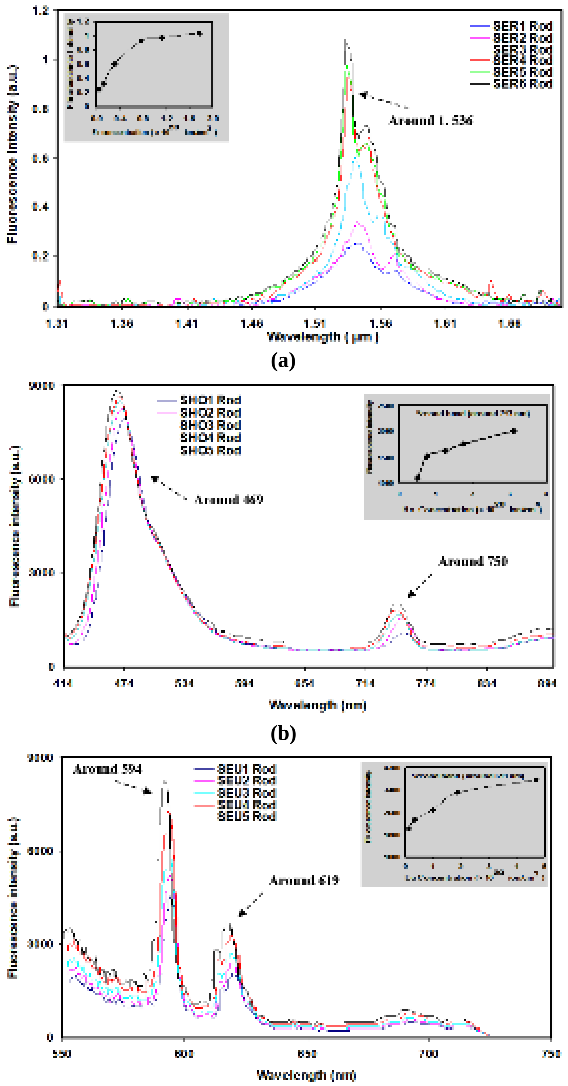

(a)

(b)

(c)

Fig. (15) Fluorescence spectra of sol-gel silica glass samples doped with different concentrations of (a) Er^{3+} , (b) Ho^{3+}, (c) Eu^{3+} and Al co-doping at Al:RE ratio of 10:1

The Er^{3+} fluorescence around 1.536 µm is clearly observed, as shown in Fig. (15a), and results from the intra-4f electric dipole transition from the first excited state $^4\boldsymbol{I}_{13/2}$ to the ground state $^4\boldsymbol{I}_{15/2}$. The two peaks result from Stark splitting of the Er^{3+} levels and characteristics for Er^{3+} in SiO$_2$ network [19]. In Fig. (15b) the fluorescence spectra of Ho^{3+} samples composed of two emission bands corresponding to ($^5G_6\rightarrow {}^5I_8$, ~469 nm) and ($^5S_2\rightarrow {}^5I_7$, ~750 nm) electric dipole transitions. Two fluorescence bands are observed, as shown in Fig. (15c), and correspond to the intra configurational $^5D_0\rightarrow {}^7F_J$ (J=1,2) spin forbidden 4f transitions of the Eu^{3+} ions. The ($^5D_0\rightarrow {}^7F_1$) transition band is at around (594 nm) and attributed to the parity-allowed magnetic dipole transition because $|\Delta S|=1$, $|\Delta L|=1$ and $|\Delta J|=1$. In contrast, the ($^5D_0\rightarrow {}^7F_2$) transition band peaking at around (619 nm) is attributed to the electric dipole transition.

It can be seen from Fig. (15) that the peak fluorescence intensity increases as the concentration of RE^{3+} ions increases. This can be attributed to the increase of the absorbed intensity (I_a) (i.e. increase the concentration of excited ions) causing corresponding increase of fluorescence intensity (I_f) which is proportional to I_a ($I_f\ \alpha\eta\ I_a$), where η is the fluorescence quantum efficiency [20]. The corresponding increases of (I_f) can occur only if the probability of radiative emission is higher than the probability of non-radiative relaxations. This condition is achieved by adding the Al co-doping with optimum ratio of 10 which enhances a good distribution of RE^{3+} ions in the silica network, reducing the tendency of these ions to cluster and subsequently the non-radiative relaxations, then results in an increase in (I_f) and reduce concentration quenching at high doping levels. The details of the Al effect are discussed later in another section. The inset of Fig. (15a) indicates that the maximum concentration (2.547% Er^{3+}) in the present work is the saturation limit [21].

The fluorescence emission intensity of the RE ions in sol-gel silica glass gives a primary indication that this system may act as a solid state laser active media. Because of the shielding of the 4f electrons from the environment, a change in the environment of the RE^{3+} ion do not affects the intensities of the observed transition very much. However, some transitions are very sensitive to small changes in the environment. These transitions are called *hypersensitive transitions* which are obeying the selection rules: $|\Delta S|=0$, $|\Delta L|\leq 2$ and $|\Delta J|\leq 2$ [22]. In the visible range, the $^5G_6\rightarrow {}^5I_8$ transition of Ho^{3+} ions peaking at around 469 nm represents the hypersensitive transitions. This may be explain the strongest emission of this transition compared to the $^5S_2\rightarrow {}^5I_7$ transition.

The strongest emission of the $^5D_0\rightarrow {}^7F_1$ transition relative to the $^5D_0\rightarrow {}^7F_2$ transition of Eu^{3+} ions suggests that the emitted light has not a pure red color. The evidence of this suggestion is appeared through the orange view of one of Eu^{3+} samples after irradiation with a UV-light source (366 nm) as shown in Fig. (16a). This result is opposite to a previous research [22], which noted that the intensity ratio I ($^5D_0\rightarrow {}^7F_2$) / I ($^5D_0\rightarrow {}^7F_1$) is a high ratio. Such a high ratio is only possible when the Eu^{3+} ions do not occupy a site with inversion symmetry, and means that the emitted light has a pure red color as shown in Fig. (16b).

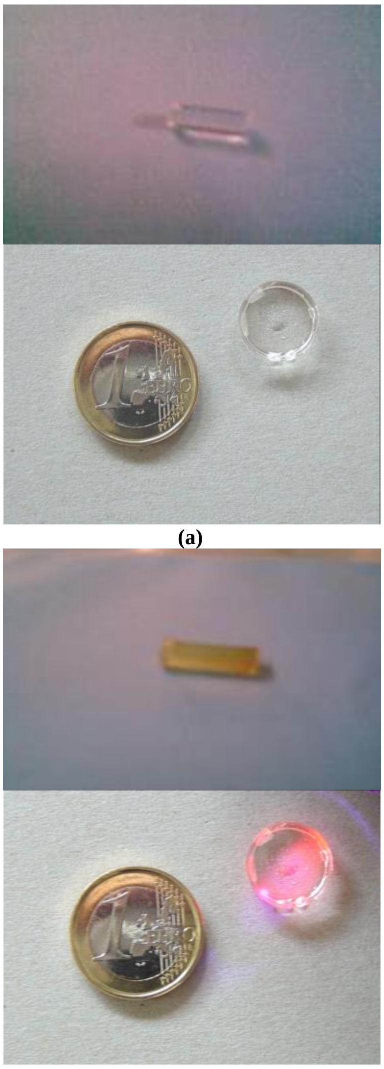
(a)

(b)

Fig. (16) Photos of the Eu^{3+}-doped sol-gel glass with and without UV-light exposure, (a) in reference [1], (b) in the present work

It can also be seen that the maximum wavelength ($\lambda_{Fmax.}$) is slightly shifted towards shorter wavelength (blue shift) in the direction of increasing RE^{3+} concentration. This blue shift at higher RE^{3+} concentrations may be ascribed to variations in the host field around Er^{3+}, Ho^{3+} and Eu^{3+} ions, which perturb the lowest Stark component of the emission state of each ion and causes the shift of spectra.

The fluorescence bands corresponding to the $^4I_{13/2}\rightarrow {}^4I_{15/2}$, $^5S_2\rightarrow {}^5I_7$, and $^5D_0\rightarrow {}^7F_2$ transitions exhibited a broad spectral width of around 46 nm, 28.3 nm and 8.5 nm at FWHM of Er^{3+}, Ho^{3+} and Eu^{3+} ions, respectively. This spectral width is due to the thermal distribution over the Stark levels and homogeneous and inhomogeneous broadening [17].

Infrared spectroscopy is the study of the interaction of infrared (IR) radiation with matter. When IR radiation interacts with matter it can be absorbed, causing the chemical bonds in the materials to vibrate. Chemical structures within molecules, known as functional groups, tend to absorb IR radiation in the same wavenumber range. The correlation between the wavenumber and molecule structures makes it possible to identify the structure of unknown molecules [23]. So that, a Fourier transform infrared (FTIR) spectroscopy is used to analyze the composition of the silica sol-gel samples.

The characteristic vibrational bands of silica were found in the FTIR spectra of Xerogel and pure sol-gel glass samples, as shown in Fig. (17), which were prepared under synthetic recipe conditions of pH 1, $\mathcal{R}$ =2 and T=60°C, drying at 110°C and sintering at 500°C only for pure sample.

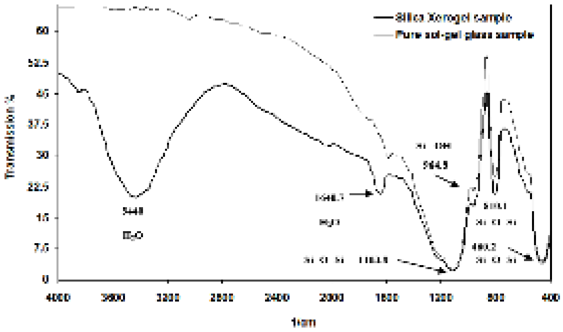

Fig. (17) FTIR transmission spectra of silica Xerogel and silica sol-gel glass

The absorption band centered at 460.2 cm^{-1} is due to the bending vibrations of (Si-O-Si) groups, and the absorption band peaking at 810.1 cm^{-1} is attributed to the symmetric stretching (Si-O-Si) groups, while the wide band at around 1103.8 cm^{-1} is the characteristic Si-O-Si asymmetric stretching vibrations [24-27]. The weak band at 964.8 cm^{-1}, which is ascribed to stretching vibration of silanol (Si-OH) groups [27], indicates the limited number of these groups in the silica network which means that the condensation reaction is nearly complete. Because of the drying process at 110°C dose not completely trap the water molecules from the pores of silica Xerogel, therefore two absorption bands appeared. The first one is at 1640.7 cm^{-1} and due to bending vibrations of (O-H) bond in H_2O molecules, while the second band peaking at 3440 cm^{-1} is ascribed to stretching vibrations of this bond [28]. However, the intensity of the first band became very weakly and the second band disappeared for the pure glass sample which is sintered at 500 °C, meaning that the most H_2O molecules are driven out after the sintering process.

Other FTIR spectra of Er^{3+}, Ho^{3+} and Eu^{3+}-doped sol-gel glass samples with Al: RE ratio of 10:1 are shown in Fig. (18). The three characteristic vibrational bands of silica, which appeared for Xerogel and pure glass samples, are found in these spectra. This gives a successful evidence of the doping process.

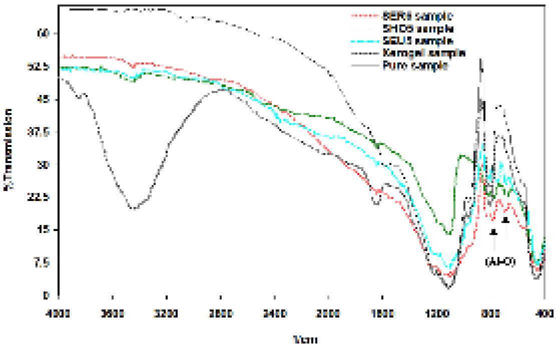

Fig. (18) FTIR transmission spectra of some of doped sol-gel glass samples

It is clear that the intensity of absorption bands near at 1640.7 cm^{-1} and 3440 cm^{-1}, which are due to bending and stretching vibrations of O-H bond, became very weak for the doped samples after sintering process. The most important result that could be seen from the FTIR spectra of doped samples is the existence of two absorption bands centered at around 684.7 cm^{-1} and 786 cm^{-1}, assigned to the presence of Al-O groups, and due to character of Al-O vibration bond [26]. In return, the intensity of absorption bands, which are due to the presence of (Si-O-Si) groups, is slightly decreases (i.e., the concentration of silica decreased). This result enhances the hypothesis that states: the Al co-doping encourages the formation of nonbrigding oxygen (NBOs), allowing the RE ions to disperse more evenly throughout the material and reducing the need to cluster [29]. Table (4) involves the functional groups with corresponding IR absorption band of silica sol-gel samples.

4. Conclusion

In concluding remarks, the effects of doping of silica glasses with rare earth element on their spectroscopic properties were studied. The silica glass monoliths were prepared by sol-gel technique and the doping process was carried out using different molar concentrations of aluminum and rare earth element (erbium). Results showed that the positions of the absorption bands in sol and bulk phases are similar to that of RE solutions, indicating the presence of RE^{3+} ions and its spectroscopic activity within the sample structure. It has also been noted that the present absorption spectra show inhomogeneous broadening which may be attributed to the amorphous character of sol-gel glass host.

References

[1] C. Vilma, L. Wander and L. Kevin, "Optical Characterization of Sol-Gel Derived from Eu^{3+} Complex-Forming Precursors", Quimica Nova, 21(3) (1998) 374-377.
[2] J. Chrusciel and L. Slusarki, "Synthesis of Nanosilica by the Sol-Gel Method and its activity

Toward Polymers", Mater. Sci. Eng. C: Mater. Biol. Appl., 21(4) (2003) 461-469.

[3] L.L. Hench and J.K. West, "The Sol-Gel Process", Chem. Rev., 90(1) (1990) 33-72.

[4] F.J. Kadhim et al., " Synthesis and spectroscopic properties of silica nanoparticles as scatter centers in random gain porous media", J. Sol-Gel Sci. Technol., 75 (2015) 247-254

[5] J.D. Mackenzie, in **"Ultrastrucuture processing of Advanced Ceramics"**, Eds. J.D. Mackenzie and D.R. Ulrich, **"Amorphous Oxides from Gels"**, John-Wiley & Sons (NY, 1984), Ch. 43, pp. 589-601.

[6] K.D. Keefer and D.W. Schaefer, "Growth of Fractally Rough Colloid", Phys. Rev. Lett., 56(22) (1986) 2376-2379.

[7] J. Laegsgaared, "Dissolution of Rare–Earth Clusters in SiO_2 by Al/Co-Doping", Phys. Rev. B, 65(17) (2002) 174114.

[8] F.J. Kadhim et al., "Photoluminescence analysis for terbium β-diketonate complex-based silica xerogel matrices", J. Sol-Gel Sci. Technol., 76 (2015) 150-155

[9] F.J. Kadhim and N.H. Al-Lamey, " Synthesis of Tb-doped titanium dioxide nanostructures by sol–gel method for environmental photocatalysis applications", J. Sol-Gel Sci. Technol., 81 (2017) 276-283.

[10] R.K. Iler, **"The Chemistry of Silica Solubility, Polymerization Colloid and Surface Properties and Biochemistry"**, John-Wiley & Sons (NY, 1979), p.172, 400.

[11] A. Kailer, G. Klaus and G. Yury, "Raman Microspectroscopy of Nanocrystalline and Amorphous Phases in Hardness Indentations", J. Raman Spectro., 30 (1999) 939-946.

[12] V.F. Tooley, **"The Hand Book of Glass Manufacture"**, The Glass Industry Magazine (NY, 1979), vol. 1, p. 39.

[13] D.M. Boye et al., "Rare Earth Ion distribution in Sol-Gel Silicate Glasses", J. Lumin., 128(5-6) (2008) 888-890.

[14] K. Patek, **"Glass Lasers"**, Butterworth (London, 1970).

[15] J. Weber, **"CRC Handbook of Laser Science and Technology"**, vol. I: Lasers and Masers, CRC press, Inc. (Florida, 1982).

[16] D.C. Brown, **"High–Peak Power Nd:Glass Laser System"**, Springer Series in Optical Sciences, vol. 25 (NY, 1981).

[17] J. Zschokke, **"Optical Spectroscopy of Glasses"**, Reidel, Dordrecht (1986).

[18] H. Lawrence and V. Vlack, **"Elements of Materials Science",** 2nd ed., U.S.A, 1964.

[19] L.H. Slooff et al., "Erbium-Implanted Silica Colloids with 80% Luminescence Quantum Efficiency", Appl. Phys. Lett., 76 (2000) 3682-3684.

[20] C.A. Parker, **"Photoluminescence of Solutions",** Elsevier (Amsterdam, 1968), 262-267.

[21] S.H. Garofalini and G. Martin, "Molecular Simulation of the Polymerization of Silica Acid Molecules and Network Forming", J. Phys. Chem., 98(4) (1999) 1311-1316.

[22] P. Lenaert, "Covalent Coupling of Luminescent Lanthanide Complexes on Hybrid Materials and Solid Polymer Supports", Ph.D. thesis, Katholieke University, Leuven, Germany (2005).

[23] B.C. Smith, **"Fundamentals of Fourier Transform Infrared Spectroscopy"**, CRC Press (FL, 1996).

[24] D. Davazoglou and V.E. Vamvakas, "Arrangement of Si and O atoms in Thermally Grown SiO_2 Films", J. Electrochem. Soc., 150 (2003) 90-96.

[25] X. Song et al., "Synthesis of CeO_2-Coated SiO_2 Nanoparticle and Dispersion Stability of its Suspension", Mater. Chem. Phys., 110 (2008) 128-135.

[26] G.C. Righini and M. Ferrari, "Photoluminescence of Rare-Earth–Doped Glasses", Rivista Del Nuovo Cimento, 28 (2005) 121-126.

[27] L. Yang, "Fabrication and Characterization of Microlasers by Sol-Gel Method", Ph.D. thesis, California Institute of Technology (2005), 43-47.

[28] C. Carla et al., "Eu^{3+}-Doped Y_2O_3-SiO_2 Nanocomposite Obtained by a Sol-Gel Method", Mat. Res. Soc. Symp. Proc., 676 (2001) 181-186.

[29] A.J. Silversmith et al., "Rare-Earth Ion Distribution in Sol-Gel Glasses Co-Doped with Al^{3+}", J. Lumin., 128(5-6) (2008) 931-933.

Table (1) Results of the atomic absorption analysis for (RE^{3+}: sol-gel glass: with Al co-doping) system. All samples derived from the molar concentration ratio Al:RE of 10:1

Sample no.	Practical Concentrations		Measured Concentrations (Atomic absorption analysis)			
	%Al $^{3+}$	%RE ion	%Al $^{3+}$	%RE ion	Al^{3+} ion density ×10^{21} cm^{-3}	RE ion density × 10^{20} cm^{-3}
SER1	0.186	0.115	0.179	0.110	0.0499	0.0498
SER2	0.438	0.274	0.402	0.248	0.1260	0.1254
SER3	1.003	0.622	0.989	0.613	0.3148	0.3151
SER4	2.180	1.351	2.040	1.264	0.7607	0.7604
SER5	2.966	1.839	2.682	1.657	1.1410	1.1307
SER6	4.246	2.632	4.110	2.547	1.7583	1.7582
SHO1	1.803	1.102	1.764	1.076	0.4890	0.4881
SHO2	2.637	1.612	2.590	1.583	0.7411	0.7407
SHO3	3.673	2.245	3.610	2.206	1.2620	1.2614
SHO4	4.850	2.956	4.251	2.600	1.7602	1.7600
SHO5	6.961	4.255	6.582	4.023	3.1148	3.1145
SEU1	0.438	0.245	0.409	0.228	0.1273	0.1276
SEU2	0.932	0.520	0.910	0.509	0.3191	0.3190
SEU3	2.911	1.628	2.780	1.555	0.9833	0.9834
SEU4	4.595	2.571	4.280	2.395	1.8590	1.8581
SEU5	10.336	5.747	10.120	5.663	4.7150	4.7152

Table (2) Characteristics & density measurements of sol-gel glass rod samples

Sample no.	Diameter (cm)	Length (cm)	Weight (gm)	True volume (cm$^{3)}$	Density (gm.cm^{-3})
Dense Xerogel	0.37	1.30	0.1743	0.148	1.177
SER1	0.40	1.31	0.1993	0.159	1.254
SER2	0.39	1.30	0.2120	0.151	1.254
SER3	0.40	1.32	0.2321	0.162	1.433
SER4	0.39	1.40	0.2673	0.160	1.671
SER5	0.39	1.43	0.3138	0.165	1.902
SER6	0.40	1.45	0.3431	0.179	1.917
SHO1	0.38	1.40	0.1915	0.154	1.244
SHO2	0.40	1.39	0.2179	0.170	1.282
SHO3	0.39	1.45	0.2615	0.167	1.566
SHO4	0.40	1.45	0.3303	0.178	1.856
SHO5	0.40	1.50	0.3837	0.181	2.120
SEU1	0.40	1.30	0.2204	0.158	1.395
SEU2	0.40	1.35	0.2593	0.165	1.572
SEU3	0.38	1.20	0.2076	0.131	1.585
SEU4	0.40	1.40	0.3288	0.169	1.946
SEU5	0.40	1.43	0.3654	0.175	2.088
Melt- silica glass	-	-	-	-	2.2 [63]

Table (3) Vickers hardness measurements of sol-gel glass rod samples

Sample no.	Impression diagonals (µm)			Vickers hardness (GPa)
	Base 1	Base 2	Side area	
Pure sol-gel glass	31	31	31.1	1.89
SER1	28.8	28.7	28.9	2.19
SER2	28.4	28.4	28.7	2.25
SER3	28.4	28.1	28.5	2.26
SER4	28.6	28.5	28.5	2.23
SER5	28.5	28.4	28.2	2.25
SER6	28.7	28.3	28.6	2.20
SHO1	29.2	29.2	29.4	2.13
SHO2	29.1	29.4	29.0	2.13
SHO3	29.1	28.7	29.2	2.14
SHO4	29.0	29.1	29.0	2.16
SHO5	28.9	28.8	29.0	2.17
SEU1	29.7	29.7	29.8	2.06
SEU2	29.9	29.5	29.9	2.03
SEU3	29.5	29.5	29.7	2.08
SEU4	29.3	29.2	29.2	2.13
SEU5	29.6	29.7	29.4	2.07
Silica glass rod	17.1	17.1	17.0	6.23
Fused silica	-	-	-	9.0 at (0.98 N) load [62]
SF7 a flint silicate glass	-	-	-	5.4 at (0.98 N) load [62]

Table (4) Infrared bond positions (cm^{-1}) for silica sol-gel glass system

Sample	IR absorption bands (cm^{-1})					
	Si-O-Si bending	Si-O-Si sym. stretching	Si-O-Si asym. stretching	Si-OH Stretching	O-H bending & stretching	Al-O vibration
Xerogel	460.2	810.1	1103.8	964.8	1640.7, 3440	-
Pure glass	460.5	810.0	1104.0	964.4	1632.0, -	-
SER1	460.5	811.4	1109.6	964.4	1640.5, 3439	684.6, 786
SER2	460.4	811.0	1109.3	964.6	- , 3440	684.6, 787
SER3	460.6	811.1	1109.3	964.4	1640.0, 3440	684.1, 787
SER4	461.0	811.5	1109.4	964.4	1640.0, -	684, 787.5
SER5	460.4	811.5	1109.5	964.3	1640.5, 3440	684.1, 787
SER6	460.0	811.0	1109.3	964.0	1640.5, 3440	684.5, 787
SHO1	460.0	813.0	1104.2	964.5	1640.0, 3440	683.2, 786
SHO2	460.4	813.0	1104.6	964.5	1640.1, 3440	683.0, 786
SHO3	460.1	813.3	1104.3	964.5	1640.2, -	683.2, 785
SHO4	460.3	813.0	1104.3	964.4	1640.0, 3440.5	683, 784.3
SHO5	460.1	813.1	1102.0	964.9	1640.5, 3441	684.4, 785
SEU1	458.0	810.6	1108.1	964.4	1639.5, -	684.2, 786
SEU2	458.0	810.1	1108.3	964.5	1639.9, -	684.1, 787
SEU3	458.0	810.5	1108.3	964.4	1639.3, 3441	684.0, 786
SEU4	457.9	810.3	1108.4	964.4	1639.7, -	684.1, 786
SEU5	457.8	810.0	1109.1	964.8	1640.0, 3440.4	684.6, 786

IRAQI JOURNAL OF APPLIED PHYSICS
Vol. 16, No. 3, July-September 2020, pp. 13-20

Effects of Operation Parameters on Structures and Surface Morphology of Tin Dioxide Nanostructures Prepared by DC Reactive Sputtering

Fuad T. Ibrahim

*Department of Physics,
College of Science,
University of Baghdad,
Baghdad, IRAQ*

In this work, tin dioxide thin films were prepared by dc reactive sputtering technique. These film were deposited on glass substrates and their structural characteristics were determined by the x-ray diffraction (XRD) patterns, atomic force microscopy (AFM) and scanning electron microscopy (SEM). It is found that the XRD peaks becomes gradually sharper with increasing discharge current that indicates smaller particle size. The AFM results showed that the prepared films have granular structure and high surface area, which is very useful for gas sensing devices based on nanostructured SnO_2 thin films. As the partial amount of oxygen in the argon:oxygen mixture is increased, the surface mobility and the energy of the SnO_2 molecules increase leading to higher mean free path of the SnO_2 molecules and hence more massive grain sizes.

Keywords: Nanostructures; DC sputtering; Tin dioxide; Surface morphology
Received: 22 May 2020; **Revised:** 28 June 2020; **Accepted:** 4 July 2020

1. Introduction

Physical adsorption (physisorption) is defined as an adsorption event where no geometric change occurs to the adsorbed molecule and van der Waals forces are involved in the bonding between the surface and adsorbate [1-3]. Chemical adsorption (chemisorption) is the formation of a chemical bond between the molecule and the surface during the adsorption process and requires activation energy (e.g. ~0.5eV for chemisorption of oxygen on SnO_2) [4,5]. Chemisorption is a much stronger bond than physisorption. Two types of chemisorption occur on the surface of metal oxides: (1) molecular chemisorption, in which all the atomic bonds are preserved in the adsorbed molecule; and (2) dissociative chemisorption, where bonding within the adsorbed molecule decomposes and molecular fragments or ions are bound to oxide surface [6,7]. Molecular chemisorption is the most probable type of adsorption for molecules that possess free electrons or multiple bonds [8]. Gas molecules with single bonds tend to react via dissociative chemisorption; however; there is an activation energy associated with dissociation [9]. The type of chemisorbed oxygen on the surface of a metal oxide is dependent on the temperature of the system. The results of oxygen adsorption on SnO_2 and correlated the adsorbed oxygen species to temperature where techniques such as infrared spectroscopy and temperature programmed desorption were used [10].

2. Experimental Part

The SnO_2 films were deposited on glass substrates, which were cleaned in alcohol, distilled water and dried in air before loading into the deposition chamber. The substrates were cleaned in sputtering of Ar plasma at bias voltage of 1000 V for 5 minutes.

The thickness of SnO_2 thin films was measured by using an optical interferometer method employing He-Ne laser (0.632μm) at incident angle of 45°. This method depends on the interference of the laser beam reflected from thin film surface and the substrate, the films thickness (t) was determined using the following formula [11]

$$t = \frac{\lambda}{2} \cdot \frac{x_2}{x_1} \qquad (1)$$

where x_1 is the fringe width, x_2 is the distance between two fringes and λ is the wavelength of laser light

The prepared thin films were examined by Bruker D2 PHASER XRD technique with Cu-Kα x-ray tube (λ = 1.54056Å). The x-ray scans were recorded with the diffraction angle in the range 20-60°. The overall structure of thin films, including lattice constants, grain size identification of unknown materials, orientation of single crystals, and orientation of the crystallites were determined. The surface topography of the prepared surfaces was investigated by the atomic force microscopy (AFM) in order to confirm the formation of nanostructures within the prepared samples.

Optical measurements on the prepared thin films were performed using a UV/Visible 2601 Lambda spectrophotometer. During scanning, a blank glass slide was placed in one of the beam's direction and another glass slide with deposited film was in the other beam's direction. Thus, the absorption spectrum displayed by the UV/Visible spectrophotometer was as a result of the films deposited on the glass slide substrates.

3. Results and Discussion

X-ray diffraction was used to study the crystal structure of SnO_2 thin films, growth on glass substrate with different; discharge current (I_d), gas pressure, and argon/oxygen mixed flow. Thin films of pure tin oxide, were investigated for their structural and surface morphological properties. Figures (1), (2) and (3) show the XRD patterns of the prepared SnO_2 thin films and table (1) shows the summary of the structural parameters obtained from the XRD patterns.

Table (1) Comparison between the experimental (Exp.) and standard (Std.) values of d_{hkl} for the peaks shown in XRD patterns for different discharge currents

I (mA)	2θ (Deg.)	FWHM (Deg)	Int. (Arb. Unit)	d_{hkl} Exp.(Å)	d_{hkl} Std.(Å)	hkl	G.S (Å)
10	-	-	-	-	-	-	-
15	-	-	-	-	-	-	-
20	26.521	0.81	280	3.358	3.3498	(110)	95
	33.214	0.79	70	2.695	2.6440	(101)	98
	51.233	1.35	40	1.778	1.7642	(211)	62
	57.751	1.37	20	1.595	1.5932	(002)	62
25	26.321	0.80	130	3.383	3.3498	(110)	97
	33.571	0.68	270	2.667	2.6440	(101)	115
	37.120	1.14	30	2.420	2.3687	(200)	69
	51.353	1.03	50	1.778	1.7642	(211)	80
	57.721	0.95	110	1.596	1.5932	(002)	90

Figure (1) shows the XRD of SnO_2 thin films were prepared at different discharge currents (10, 15, 20, and 25 mA), all SnO_2 thin films deposited on glass substrate under same conditions, mainly, the inter-electrode distance is 5 cm, the sputtering pressure is $5x10^{-2}$ mbar and sputtering time is 60 min. The diffraction pattern of the sample A and B as shown in Fig. (1) has no peaks which indicates the amorphous nature of the film. In sample C and D randomly oriented tin oxide crystalline formation starts and planes corresponding to (110), (101) and (211) appear crystal lattice planes and all other smaller peaks coincide with the tetragonal rutile structure of SnO_2. The presence of broad and weak peaks indicate that SnO_2 has very crystalline size or that SnO_2 particles are semi-crystalline in nature [12]. The unit cell consists of two metal atoms and four oxygen atoms. Each metal atom is situated a middle six oxygen atoms which approximately form the corners of a regular octahedron. Oxygen atoms are surrounded by three tin atoms which approximate the corners of an equilateral triangle. It is found that the XRD peaks becomes gradually sharper with increase in discharge current, indicating smaller particle size. Intensities corresponding to (110), (101) and (211) get enhanced with discharge current showing better crystallinity of films deposited at higher discharge current. In sample D an enhanced intensity shift toward (101) from (110) plane and a new peaks corresponding to (200) and (220) plans are seen. A disappearance of XRD peaks corresponding to some lattice planes may be caused by large number of vacant lattice sites or locale lattice disorders [13]. The calculated lattice parameters of as prepared SnO_2 thin films are given in table (2).

Table (2) Comparison of lattice constant showed in XRD for different discharge current

Discharge current (mA)	a (Å)	c (Å)	Calculated density (gm/cm^3)
10	-	-	-
15	-	-	-
20	4.7012	3.190	7.07
25	4.7362	3.192	6.96

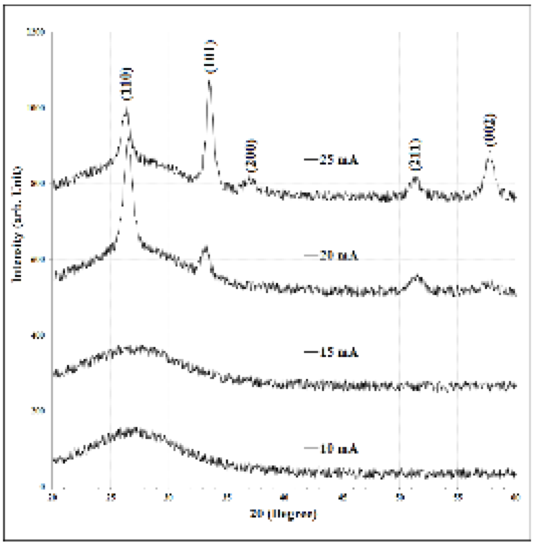

Fig. (1) XRD of sputtering SnO_2 thin films on glass substrate for different discharge currents

The XRD patterns of the deposited SnO_2 thin films using different working pressures (0.015 to 0.15 mbar), argon:oxygen mixing ratio of 1:2, sputtering time of 60 min, inter-electrode distance of 5 cm, biasing voltage of 4 kV, are shown in Fig. (2).

Reflections from the tetragonal crystallographic phase (cassiterite) of SnO_2 became more defined and progressively more intense and sharp for films with increasing of working pressures. In all samples randomly oriented tin oxide crystalline formation starts planes corresponding to (110), (101), (211) and (002) planes of SnO_2 for 2 θ values of 26.51, 33.85, 51.69 and 57.93, respectively.

From Fig. (2) and tables (3) and (4), its clear that the films are textured and the degree of texturing depends on the value of working pressure. The change of predominant orientation of crystallites, forming gas sensitive matrix, and confirms the cassiterite structure of nanocrystalline SnO_2 [14]. The (110) is the dominant crystal structure of low-index crystal faces for this material due to its stability. This is the desired structure of SnO_2 for sensing applications since its prevalent (110) growth plane is extremely stable and can reject oxygen with little distortion [15]. The growth of this plane helps in achieving high oxygen vacancy concentrations at low temperature.

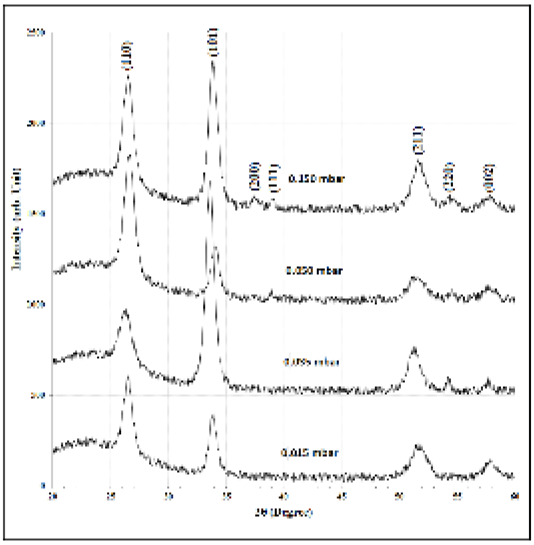

Fig. (2) XRD of sputtered SnO_2 thin films on glass substrate for different working pressure

Table (4) Comparison lattice constant showed in XRD for different discharge current

Pressure (mar)	a (Å)	c (Å)	Calc. density (gm/cm^3)
0.015	4.750	3.182	6.94
0.035	4.789	3.192	6.81
0.050	4.731	3.188	6.98
0.150	4.749	3.190	6.92

Crystal structure of films was characterized by X-ray diffraction. The XRD pattern of SnO_2 thin films deposited on glass substrate for different Ar:O_2 mixing ratios (4:1, 2:1, 1:1, 1:2 and 1:4) at optimum constant working pressure of 0.05 mbar, sputtering time of 60 min, inter-electrode distance of 5 cm, and biasing voltage of 4 kV, as shown in Fig. (3). All films are polycrystalline and the preferred orientation is in (110) direction for the films deposited using mixing ratio lower than 1 (i.e., 1:2 and 1:4). The preferred orientation was changed from (110) to (211) as the mixing ratio increased from 1 to 4.

Tables (5) and (6) demonstrate significant changes in grain size as well as in intensity of peaks. These changes are due to increase the reaction between the oxygen and the Sn target surface. On the other hand, with increased oxygen atoms, the substrate film surface would be absorbed on, to produce the (110) dominant crystal structure.

Table (6) Comparison lattice constant showed in XRD for different Ar to O2 mixed flow.

Ar/O_2	a (Å)	c (Å)	Calc. density (gm/cm^3)
1/4	4.783	3.206	6.79
1/2	4.755	3.184	6.92
1/1	4.791	3.192	6.80
2/1	4.772	3.192	6.85
4/1	4.783	3.186	6.84

The increasing of oxygen content is related to a significant increase of the density of defects. The increase in the oxygen absorption might be attributed to a change in film structure from an amorphous film containing the Sn_2O_3 phase towards a mixed phase containing SnO and SnO_2 with a large density of defects. Due to the presence of the SnO phase, the average transmission in the visible was decreased. The SnO phase is leading to the brownish color of the films which is characteristic for SnO [16]. However, the film structure is not suited to ensure a high conductivity, as confirmed by the high resistivity observed.

AFM is used to study the surface morphology with resolution of 0.1 nm. The roughness of the coated surface is an important parameter, where the surface roughness not only describes the light scattering but also gives an idea about the quality of the surface under investigation, in addition to providing some insight on the growth morphology. Two and three-dimensional AFM images of the as-deposited SnO_2 films with different discharge current, working gas pressure, and Ar/O_2 mixture flow are shown in Figs. (4), (5) and (6), respectively. The average grain size and root mean square roughness (RMS) of these films are shown in table (7). The AFM images of all samples displayed are granular structure. The granular films show higher surface area, which is conductive for film-gas interaction and results in higher gas sensitivity [17]. The gas sensitivity has a proportional relationship with film roughness [18].

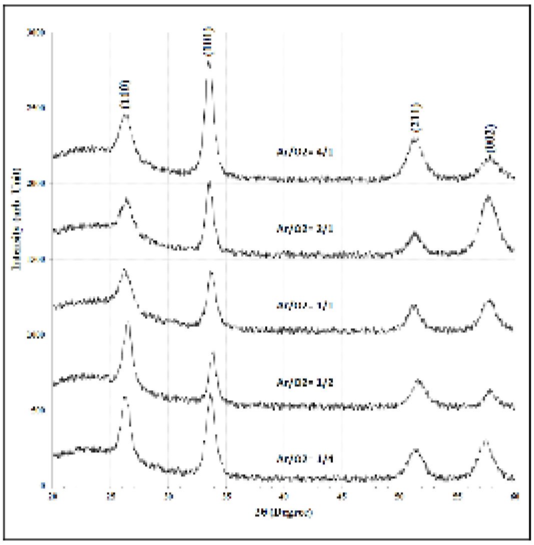

Fig. (3) XRD of sputtered SnO_2 thin films on glass substrate for different Ar to O_2 mixed flow

Figure (4) shows that the average grain size and average roughness increase from 86.14 nm and 0.0301 nm for discharge current 10 mA to 109.1 nm and 0.203 nm for discharge current 25 mA. These small grain sizes are uniformly distributed of shape and size along the film surface, with tight packed grains is observed. The increasing discharge current increased thermal energy for further increase in substrate temperature, which enhances the mobility of the atoms on the surface further to form even larger grains. As they form larger grains, the surface roughness also increases due to the formation of deeper edges. Or the roughness and average grain size was increased as the substrate temperature increase.

Figure (5) shows the decreasing in grain size from 138.29 nm at pressure 0.15 mbar to 78.73 nm at pressure 0.035 mbar and increases after that, while the roughness increases from 1.08 nm at 0.15 mbar to 1.85 nm at 0.035 mbar and decreases after that. The low dense plasma which have not enough energy to re-nucleation which leads to increase the average roughness and decreases grain size.

All images appeared in Fig. (6) show homogeneous cluster distribution with columnar structure; where the average grain size values decrease slightly with increasing of oxygen flow. Increasing oxygen flow leads to increasing in number of oxygen molecules adsorbs on the substrate surface which act as traps for atoms causing to reduce grain size for thin films by increasing in the number of nucleation centers, Also, increases roughness with increasing oxygen flow which leads to increase the vertical growth on substrate surface.

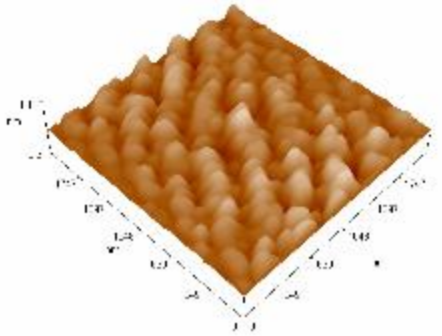

I_d=10mA

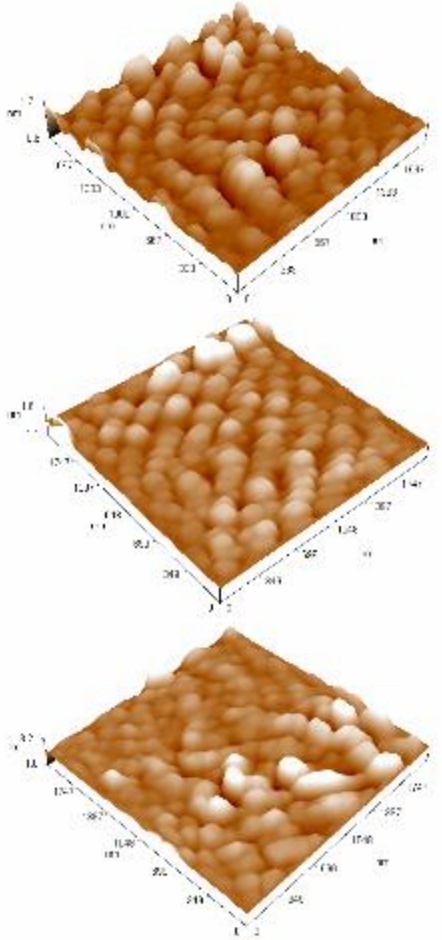

Fig. (4) The AFM images of SnO_2 thin films deposited on glass substrate for different discharge current

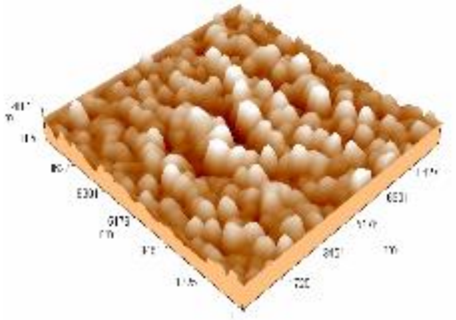

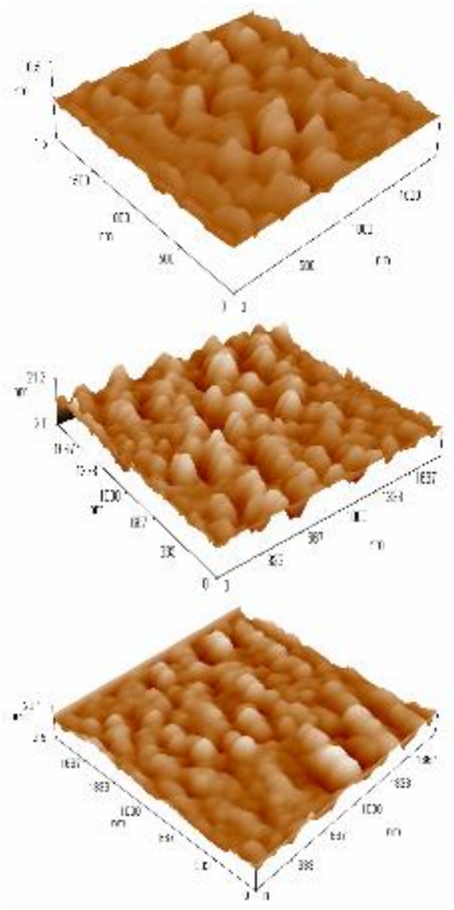

Fig. (5) The AFM images of SnO_2 thin films deposited on glass substrate for different gas pressure

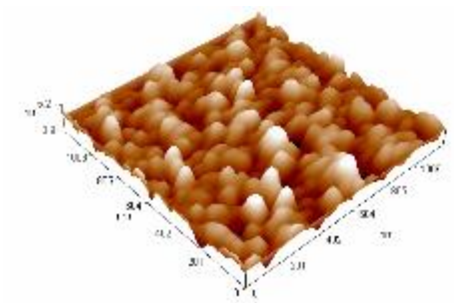

Ar/O_2=4/1

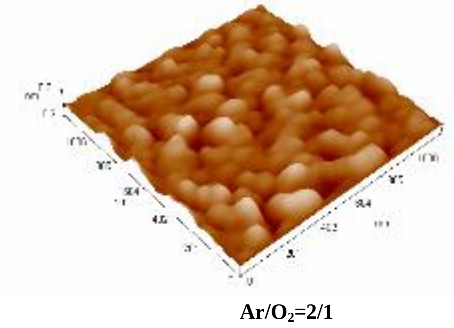

Ar/O_2=2/1

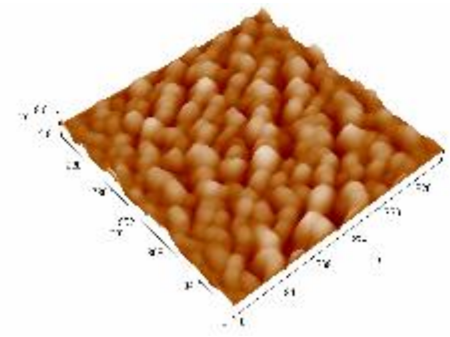

Ar/O_2=1/1

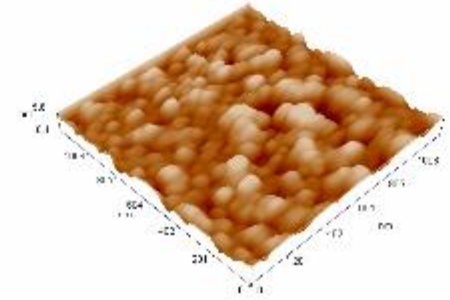

Ar/O_2=1/4

Fig. (6) The AFM images of SnO_2 thin films deposited on glass substrate for different Argon/Oxygen mixture flow

The SEM images in Fig. (7) show surface morphology of SnO_2 films grown on glass substrates under sputtering applied voltage 4kV, and 2/1 ,1/4 argon-oxygen mixture gas. It can be seen that SnO_2 films grown at 1/4 mixed gases ratio are composed of tiny grains with uniform diameters around 44.66 nm. While the grain sizes increased as increased argon-oxygen mixture gases, resulting in blend of dissimilar grain sizes. The grain sizes around 55.82nm in film grown at (2/1) mixed gas. Similar enlargement of the grain size at different argon-oxygen mixture are found in other working [19] and were explained as that when the argon-oxygen mixture increased, the surface mobility and the energy of the SnO_2 molecules increase, leading to higher mean free path of the SnO_2 molecules and hence more massive grain sizes.

Table (7) shows the surface morphology details of a film nanostructure determined by means of the AFM method with different deposition conditions. AFM characterization of the films surfaces revealed a granular, polycrystalline morphology with grain size and roughness. Also the grain size of AFM images was compared with scan electron microscope (SEM) image, which is demonstrated in Fig. (8) for two samples.

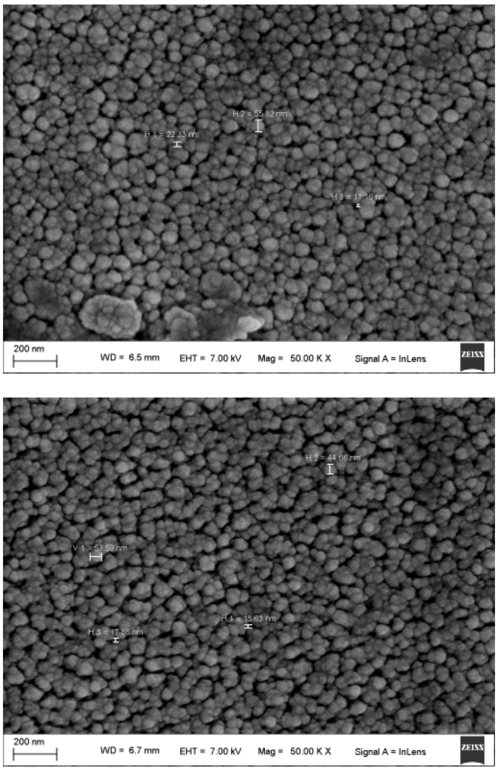

Fig. (7) The SEM images of SnO_2 thin films deposited on glass substrate at 0.05 mbar gas working pressure (a) $Ar/O_2=2/1$ (b) $Ar/O_2=1/4$

4. Conclusion

In concluding remarks, tin dioxide thin films were prepared by dc reactive sputtering technique. These film were deposited on glass substrates. It is found that the XRD peaks becomes gradually sharper with increasing discharge current that indicates smaller particle size. The AFM results showed that the prepared films have granular structure and high surface area, which is very useful for gas sensing devices based on nanostructured SnO_2 thin films. As the partial amount of oxygen in the argon:oxygen mixture is increased, the surface mobility and the energy of the SnO_2 molecules increase leading to higher mean free path of the SnO_2 molecules and hence more massive grain sizes.

References

[1] J. Hildenbrand, "Simulation and characterization of a micro machined gas sensor and preparation for model order reduction", Diploma thesis, Albert Ludwig University, Freiburg, Germany, (2003).

[2] G.E. Patil et al., “Synthesis characterization and gas sensing performance of SnO_2 thin films prepared by spray pyrolysis”, Bull. Mater. Sci., 34(1) (2011) 1-9.

[3] C. Xu et al., “Grain size effects on gas sensitivity of porous SnO_2-based elements”, Sensors and Actuators B, 3(2) (1991) 147-155.

[4] E.R. Beac, "Picoliter drop deposition of oxide nano-particles: a route to high performance micro sensor arrays", Ph.D. dissertation, The Ohio State University, (2009).

[5] W.S. Hu et al., “Preparation of nanocrystalline SnO_2 thin films used in chemisorption sensors by pulsed laser reactive ablation”, J. Mater. Sci.: Materials in Electronics, 8 (1997) 155-158.

[6] M. Gaidi et al., “Structure and photoluminescence of ultrathin films of SnO_2 nanoparticles synthesized by means of pulsed laser deposition”, J. Appl. Phys., 108(6) (2010) 063537.

[7] T.W. Kim, D.U. Lee and Y.S. Yoon, “Microstructural, electrical, and optical properties of SnO_2 nanocrystalline thin films grown on InP (100) substrates for application as gas sensor”, J. Appl. Phys., 88(6) (2000) 3759-3761.

[8] J. Gong et al., “Development of Micromachined Nanocrystalline Mesoporous SnO_2 Gas Sensor for Electronic Nose”, IEEE Proc., 7803 (2003) 124-128.

[9] J. Kaur, S.C. Roy and M.C. Bhatnagar, “Highly sensitive SnO_2 thin film NO_2 gas sensor operating at low temperature”, Sensors and Actuators B, 123 (2007) 1090-1095.

[10] N. Barsan and U. Weimar, "Understanding the fundamental principles of metal oxide based gas sensors; the example of CO sensing with SnO_2 sensors in the presence of humidity", J. Phys.: Cond. Matter, 15 (2003) 813-839.

[11] K.L. Chopra, “Thin Film Phenomena”, McGraw-Hill (NY, 1969).

[12] Z. Chen et al., “Insight on fractal assessment strategies for tin dioxide thin films”, Amer. Chem. Soc., 4(2) (2010) 1202-1208.

[13] Joint Committee on Powder Diffraction Standards (JCPDS), International Center for Diffraction Data, Swarthmore, card no. 36-1451, PA, (1980).

[14] G. Korotcenkov et al., “XRD study of gas sensitive SnO_2 thin films deposition by spray pyrolsis method”, Conf. Proc., vol. 1 (1999).

[15] F.R. Sensato et al., “Periodic study on the structural and electronic properties of bulk oxidized and reduced SnO_2 (110) surfaces and the interaction with O_2”, Surf. Sci., 511 (2002) 408-420.

[16] J. Boltz, “Sputtered tin oxide and titanium oxide thin films as alternative transparent conductive oxides”, Aachen, Techn. Hochsch., Diss., (2011) 62-65.

[17] S.C. Gadkari et al., “Solid state sensors for toxic gases”, Tech. Phys. Proto. Eng. Div. Bhabha Atomic Res. Centre, Issue. 49 (2005).

[18] N.G. Deshpandea et al., “Studies on tin oxide-intercalated polyaniline nanocomposite for ammonia gas sensing applications”, Sensors and Actuators B, 138 (2009) 76-84.

[19] Z.H.W. “Preparation and piezoresistive characteristics of polycrystalline SnO_2 films”, IEEE Xplore, 15 (1995) 154-157.

Table (3) Comparison between the Exp. and Std. value of d_{hkl} for the peaks showed in XRD for different gas pressure

P (mbar)	2θ (Deg.)	FWHM (Deg)	Int. (Arb. Unit)	d_{hkl} Exp. (Å)	d_{hkl} Std. (Å)	hkl	G.S (Å)
0.015	26.51	0.89	412	3.359	3.3498	(110)	86
	33.85	0.75	335	2.646	2.6440	(101)	103
	51.69	1.56	175	1.767	1.7642	(211)	53
	57.93	1.41	83	1.591	1.5932	(002)	61
0.035	26.30	1.27	285	3.386	3.3498	(110)	60
	33.61	0.85	1129	2.664	2.6440	(101)	92
	51.29	1.29	228	1.780	1.7642	(211)	64
	54.25	0.32	62	1.689	1.6749	(220)	314
	57.70	0.51	53	1.596	1.5932	(002)	167
0.050	26.63	1.024	659	3.345	3.3498	(110)	75
	34.03	0.85	265	2.632	2.6440	(101)	92
	38.98	0.22	44	2.308	2.3087	(111)	356
	51.53	1.61	134	1.772	1.7642	(211)	53
	54.50	0.61	38	1.682	1.6749	(220)	145
	57.81	1.20	68	1.594	1.5932	(002)	71
0.150	26.52	1.00	594	3.358	3.3498	(110)	76
	33.87	0.89	798	2.644	2.6440	(101)	87
	37.52	0.78	53	2.395	2.3687	(200)	101
	38.98	0.61	39	2.309	2.3087	(111)	141
	51.71	1.30	256	1.766	1.7642	(211)	62
	54.43	1.18	52	1.684	1.6749	(220)	71
	57.76	1.22	63	1.595	1.5932	(002)	69

Table (5) Comparison between the Exp. and Std. value of d_{hkl} for the peaks showed in XRD for different Ar to O_2 mixed flow

Ar/O_2	2θ (Deg.)	FWHM (Deg)	Int. (Arb. unit)	d_{hkl} Exp. (Å)	d_{hkl} Std.(Å)	hkl	G.S. (Å)
1/4	26.33	0.88	407	3.382	3.3498	(110)	87
	33.67	0.95	531	2.660	2.6440	(101)	82
	51.40	1.55	191	1.776	1.7642	(211)	54
	57.45	1.50	246	1.603	1.5932	(002)	57
1/2	26.49	0.87	417	3.362	3.3498	(110)	88
	33.85	0.74	330	2.646	2.6440	(101)	106
	51.72	1.36	166	1.766	1.7642	(211)	61
	57.86	1.18	96	1.592	1.5932	(002)	72
1/1	26.28	1.27	246	3.388	3.3498	(110)	61
	33.73	0.88	362	2.655	2.6440	(101)	88
	51.28	1.38	154	1.780	1.7642	(211)	60
	57.70	1.50	205	1.596	1.5932	(002)	57
2/1	26.39	1.21	222	3.374	3.3498	(110)	63
	33.57	0.77	465	2.667	2.6440	(101)	102
	51.35	1.55	134	1.778	1.7642	(211)	54
	57.72	1.78	377	1.596	1.5932	(002)	48
4/1	26.33	1.23	285	3.382	3.3498	(110)	62
	33.55	0.88	770	2.669	2.6440	(101)	88
	51.38	1.57	276	1.777	1.7642	(211)	53
	57.83	1.90	140	1.593	1.5932	(002)	45

Table (7) The AFM and SEM data images of SnO_2 thin films deposited on glass substrate for different condition

Discharge current (mA)	Gas pressure (mbar)	Argon/Oxygen mixture flow	Average Roughness (nm)	Average Grain Size (nm)
10	0.05	1/2	0.0301	86.14
15	0.05	1/2	0.103	79.93
20	0.05	1/2	0.0455	93.85
25	0.05	1/2	0.203	109.1
Biasing voltage (kV)	**Gas pressure (mbar)**	**Argon/Oxygen mixture flow**	**Average Roughness (nm)**	**Average Grain Size (nm)**
4	0.15	1/2	1.08	138.29
4	0.05	1/2	0.353	98.66
4	0.035	1/2	1.85	78.73
4	0.015	1/2	1.58	97.19
Biasing voltage (kV)	**Gas pressure (mbar)**	**Argon/Oxygen mixture flow**	**Average Roughness (nm)**	**AFM Average Grain Size (nm)**
4	0.05	4/1	0.613	72.22
4	0.05	2/1	0.526	71.05
4	0.05	1/1	1.58	56.91
4	0.05	1/4	0.604	60.52

IRAQI JOURNAL OF APPLIED PHYSICS
Vol. 16, No.3, July-September 2020, pp. 21-26

Terahertz Lasing Using Optically Excited Neutral Donor Centres Embedded in Crystalline Silicon

Miroslav Makarov
Alexander Timoshkov
Anatoly Borisov

Department of Physics,
Faculty of Science,
Technical University of Sofia,
Sofia, BULGARIA

In this work, the results demonstrate with the evidence the possibility to get the THz lasing using optically excited neutral donor centres embedded in crystalline silicon. The physical principles are clear and on the whole the results of the theoretical calculations taking into account both the intravalley and intervalley phonon-assisted captured carrier relaxation are in a good qualitative agreement with the experimental data, particularly for the Si:P laser. At the same time the experiment with Si:Bi revealed an unexpected delay (3×10^{-7} s) in the temporal behavior of the stimulated emission.

Keywords: Silicon devices; Laser; Shallow centers; Stumulated emission
Received: 2 June 2020; **Revised:** 19 August 2020; **Accepted:** 26 August 2020

1. Introduction

Silicon based semiconductors and semiconductor heterostructures are promising media for THz laser engineering due to the highly developed technology of silicon growth and doping, low level of lattice absorption in THz range and different ways to obtain the population inversion of charged carriers.

Historically there were several attempts to make a THz laser using intraband optical transitions in silicon. In 1979 the idea of the mechanism of the population inversion and the amplification on the transitions between light (*l*) and heavy (*h*) holes subbands of the valence band in crossed electric and magnetic ($E\perp H$) fields was proposed [1]. Since that time hot hole silicon lasing is under discussions.

Monte-Carlo calculations predicted small signal gain of 0.1 cm^{-1} on intersubband *l-h* optical transitions in Si in $E\perp H$ in the frequency range of 50-230 cm^{-1} [2]. Later it was shown that Landau level optical transitions in $E\perp H$ fields can also provide the amplification of THz radiation on the light hole cyclotron resonance (at frequency of 26 cm^{-1} at H=3T) [3,4]. In this case the required inversion population and nonequidistancy of principle Landau levels are provided due to the mixing (hybridization) of light and heavy subband states. The above mentioned laser mechanisms were successfully achieved experimentally in *p*-Ge in the frequency range of 50-140 cm^{-1} [5,6]. However, similar experimental investigations of silicon met the problem of the breakdown of the acceptors at liquid helium temperature and because of this reason was not successful. Nevertheless, positive results concerning hot hole gain in $E\perp H$ fields in silicon have been obtained recently [4].

The idea to use optically excited neutral shallow donors (D^0) for THz lasing was proposed for the first time in 1996 [7,8]. It was reported that both acoustic phonon (Si:P) and optical phonon (Si:Bi) assisted relaxation of non-equilibrium carriers under the photoionization of donors by CO_2 laser radiation leads to population inversion and the amplification on intracentre transitions for moderate level of doping ($N_D\approx10^{15}$ cm^{-3}) and low lattice temperatures ($T \leq$ 30-60 K). Later on, the theoretical model was worked out more precisely [9,10] taking into account multivalley structure of the conduction band. It was shown that the intervalley phonon assisted nonradiative transitions are very important for quantitative analysis.

Up to the moment THz lasing has been realized and laser transitions have been unambiguously identified for phosphorus-doped (Si:P) [11-13], bismuth-doped (Si:Bi) [13,14] and antimony-doped (Si:Sb) [15] silicon.

In this article, recent theoretical calculations and experimental investigations concerning THz lasing of group V shallow donor centres under their photoionization by CO_2 laser radiation are reviewed and discussed.

2. Theoretical background

Shallow donor states in silicon are originating from the six equivalent valleys (ν= 1-6) along <100> orientations in the energy structure $E_\nu(\boldsymbol{k})$ of the conduction band (see review [16]). Also, all bound impurity states except of the lowest *1s* state can be considered using a single valley effective mass theory. In the frame of such approach every state of the Coulomb centre exhibits at least a six-fold degeneracy originating from conduction band minima. However for the *1s* ground state the effective-mass theory is inadequate and the degeneracy is lifted by the crystal cell potential. The overlapping of the *1s* eigenfunctions belonging to each valley leads to the intervalley interaction (hybridization of states) and as a result to the valley orbit splitting of the *1s* state. The effect depends on the chemical nature of the impurity atom and is called the “chemical splitting“. The binding energies of the bound states of group V donors (arsenic As, antimony Sb, phosphorus P, bismuth Bi) as well as lithium Li donor are presented in Table (1). One can see that the *1s* multiplet resolves into a triplet $1s(T_2)$, a doublet *1s(E)* and a singlet $1s(A_1)$.

Table (1) **Energy levels of group V and lithium donors in silicon [16]**

Level	P	As	Sb	Bi	Li	Theory
$1s(A_1)$	45.59	53.76	42.74	70.98	31.24	31.27
1s(E)	32.58	31.26	30.47			31.27
$1s(E+T_2)$					33.02	31.27
			32.89	32.89		
$1s(T_2)$	33.89	32.67				31.27
			32.91	31.89		
$2p_0$	11.48	11.50	11.51	11.44	11.51	11.51
2s		9.11		8.78		8.83
$2p_\pm$	6.40	6.40	6.38	6.37	6.40	6.40
$3p_0$	5.47	5.49	5.50	5.48	5.49	5.49
3s				4.70		4.75
$3d_0$	3.83	3.8		3.80		3.75
$4p_0$	3.31	3.31	3.33	3.30	3.32	3.33
$3p_\pm$	3.12	3.12	3.12	3.12	3.12	3.12
4s				2.89		2.85
$4f_0$	2.33			2.36		2.33
$4p_\pm$, $5p_0$	2.19	2.19	2.20	2.18	2.20	2.19, 2.23
$4f_\pm$	1.90	1.90	1.94	1.91	1.90	1.89
$5f_0$	1.65		1.71	1.67	1.64	1.62
$5p_\pm$	1.46	1.46	1.48	1.46	1.47	1.44
$5f_\pm$	1.26				1.25	1.27
$6p_\pm$	1.09	1.07	1.10	1.08	1.07	1.04

Moreover for the substitution donors P, As, Sb, Bi the $1s(A_1)$ state is a ground state. It is shown below that donor lasing arises on the $2p_0 \rightarrow \{1s(E), 1s(T_2)\}$ allowed optical transitions in the frame of a four level scheme. Consequently the “chemical splitting” determines the laser states and is a major factor in the formation of the population inversion and the amplification of the donor transitions.

There are two mechanisms of the population inversion of donor states in silicon under photoexcitation. The first one is connected with the low temperature intracentre acoustic phonon assisted relaxation and is based on the accumulation of charged carriers in the long-living $2p_0$ state of P, Sb, As and perhaps Li neutral donor centres. For *n*-type Si active optical phonons have energies about 63 meV and 59 meV, which are larger than the binding energies of P, Sb, As and Li impurity states (see Table 1). Therefore for these donors at low lattice temperature ($T< 30\,K$) the electron-phonon interaction mediated by optical lattice vibrations is negligible and the population of the donor states under the optical excitation (Fig. 1) is controlled by acoustic phonon emission.

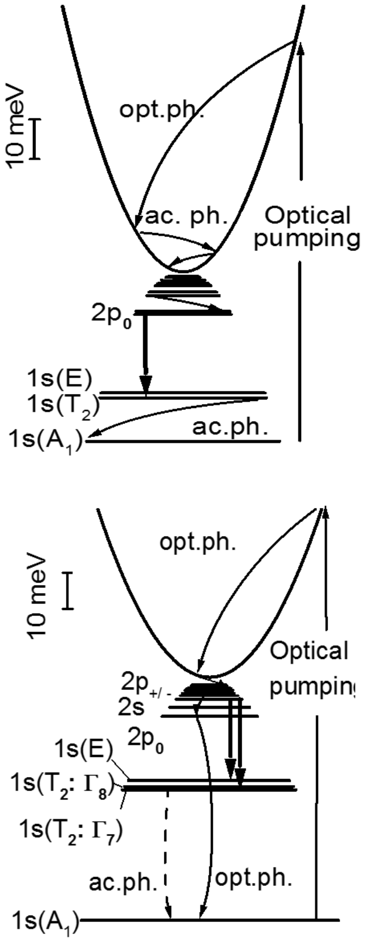

Fig. (1) The energy levels scheme and possible radiative and nonradiative transitions in Si:P (upper) and Si:Bi (lower) under the optical pumping

The matrix elements of such processes decrease with the increasing of the energy gap ΔE between corresponding levels provided $qa>1$, where a is an effective radius of the state orbit, q is a wave-vector of the phonon required for the nonradiative transition. Note, that for the long-wavelength acoustic phonons participated in the intravalley intracentre relaxation $\hbar qs = \Delta E$, where s is a speed of sound, $\hbar$ – Plank's constant. At the condition $qa>1$ the phonon-assisted transitions are ended outside of the *q*-space area where the wavefunctions of these states are mainly localized and the rate of the intravalley relaxation is suppressed with increasing *qa* parameter. As a consequence the step-by-step cascade acoustic phonon relaxation is slowing down and transitions between adjacent levels predominate at least for the lower ($n\leq3$) bound states. Moreover, the lifetime of the $2p_0$ state occurs to be the longest.

The estimation made in the frame of the single valley approximation gives the lifetime of the $2p_0$ state equal to 1.5×10^{-8}s. Therefore, the majority of excited carriers passes through the $2p_0$ state before the returning to the ground state and is accumulated there. In comparison the lifetime of the *1s(E)* state is much shorter (2×10^{-10}s) because of the smaller energy gap between this state and $1s(A_1)$ ground state. Thus the four-level laser scheme (Fig. 1) with thresholdless population inversion on the $2p_0 \rightarrow 1s(E)$ transitions can be realized. However the problem connected with a trapping of carriers on the $1s(T_2)$ state is expected within single valley approximation. On the base of group theory analysis of electron-phonon interaction [17] it was revealed that the acoustic phonon assisted intravalley relaxation is forbidden for this state. The accumulation of carriers on the $1s(T_2)$ states terminates the inversion population and the laser effect. Fortunately, the intervalley relaxation from the $1s(T_2)$ state is allowed and makes the lifetime of the $1s(T_2)$ state comparable with the lifetime of the $1s(E)$ state. Besides this, the intervalley scattering decreases the lifetime of the $2p_0$ state to 10^{-9}s [10]. Thus, it can be concluded that both inter- and intravalley acoustic phonon assisted transitions are important and have to be taken into account in the theoretical model. The results of the calculation of the involved states populations, free carrier concentration *n* and the small signal gain within the single valley approximation and with the account of the intervalley phonon assisted transitions for phosphorus donors are presented in Fig. (2) and on Fig. (3) correspondingly for comparison.

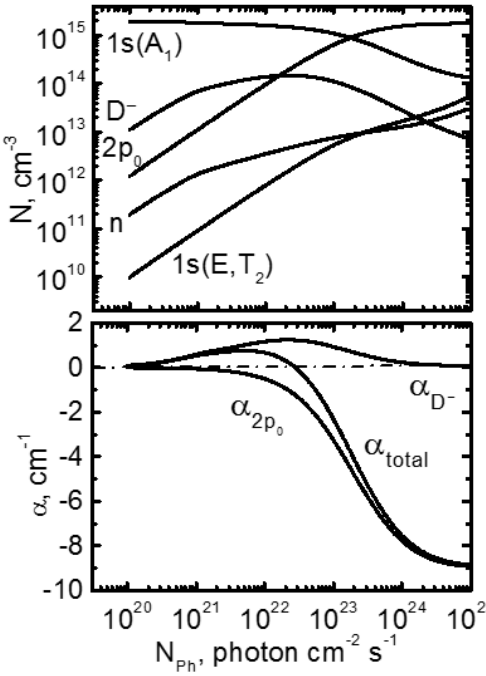

Fig. (2) The populations of donor states (upper graph) and absorption/amplification coefficient (lower graph) of Si:P calculated in the frame of single valley approximation for 2×10^{15}cm^{-3} and low compensation (0.002) versus 10.6 µm photon flux density N_{Ph}

The absorption of the THz radiation by the negatively charged donor centres (D^-) [18] created by a CO_2 laser photoionization has also been taken into account. It is shown that the typical threshold flux density for laser action is of the order of 10^{23} quantum×cm^{-2}×s^{-1} for the uncompensated samples. The optimal doping level, 10^{15}-3×10^{15} cm^{-3}, is determined by the two factors: maximum of the active centres on the one hand and, on the other hand, minimum of the impurity concentration broadening of the linewidth for the intracentre laser transition. It should be emphasised that the compensation ($K=N_d/N_a$, where N_d and N_a is the donor and acceptor concentration correspondingly) level influences the gain essentially due to the changing the absorption by the D^- centres (Fig. 4).

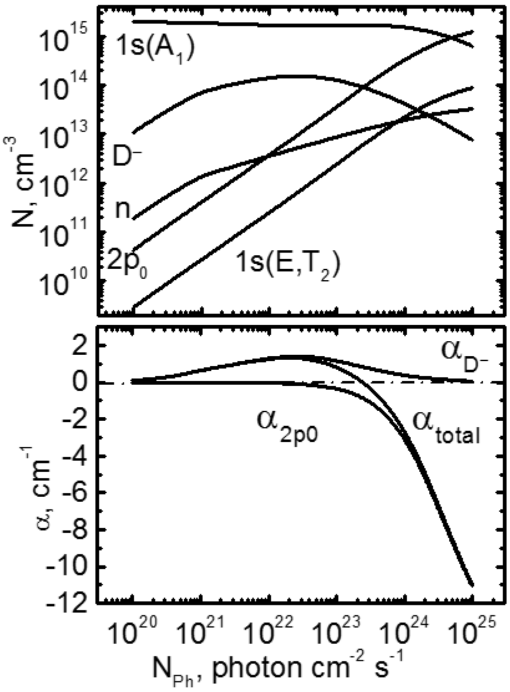

Fig. (3) The populations of donor states (upper graph) and absorption/amplification coefficient (lower graph) of Si:P calculated in the frame of intervalley approximation for 2×10^{15}cm^{-3} and low compensation (0.002) versus 10.6 µm photon flux density N_{Ph}

In contrast to silicon doped by phosphorus , where population inversion is based on the long-living $2p_0$ state, in silicon doped by bismuth the inversion is formed due to the resonant interaction with intervalley optical phonons (Fig. 1). The $2p_0$ and $2s$ states in Si:Bi are coupled to the $1s(A_1)$ state via optical phonon emission [19] and have a very short lifetime, of about 1 ps. Due to this coupling the majority of the optically excited electrons relaxes directly to the ground state and, therefore, does not reach the $1s(E)$ and $1s(T_2)$ states. As a result, the population of the $2s$ and $2p_0$ states as well as $1s(E)$ and $1s(T_2)$ states is relatively low.

The lifetime of the $2p_\pm$ state (10^{-10} s) is not longer than that of $1s(E)$, $1s(T_2)$ states (10^{-9} s), controlled by intravalley acoustic phonon assisted transitions. Nevertheless, due to the fact that the probability for excited carrier to reach the $2p_\pm$ state (0.5) is much higher then that of $1s(E)$, $1s(T_2)$ states (~10^3) the inverse population is formed between the $2p_\pm \rightarrow$

$1s(E)$, $1s(T_2)$ as well as on both $2p_{\pm} \rightarrow 2p_0$ and $2p_{\pm} \rightarrow 2s$ transitions.

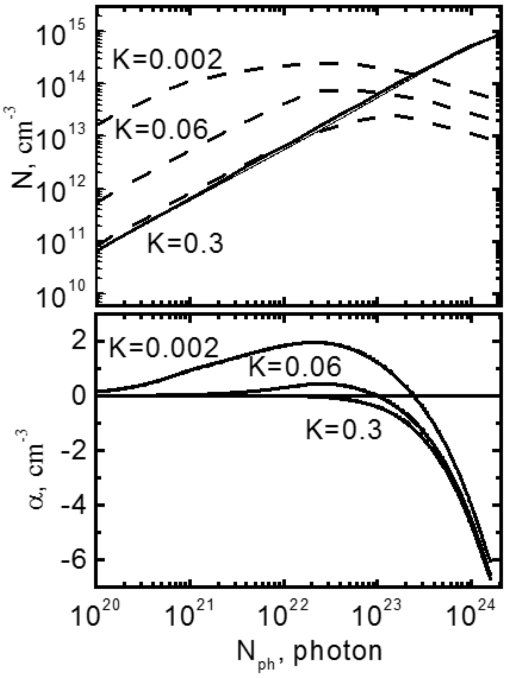

Fig. (4) The $2p_0$ (solid) and D^- centre (dash) population (upper graph) and absorption/amplification coefficient (lower graph) for different levels of compensation versus 10.6 µm photon flux density N_{Ph}

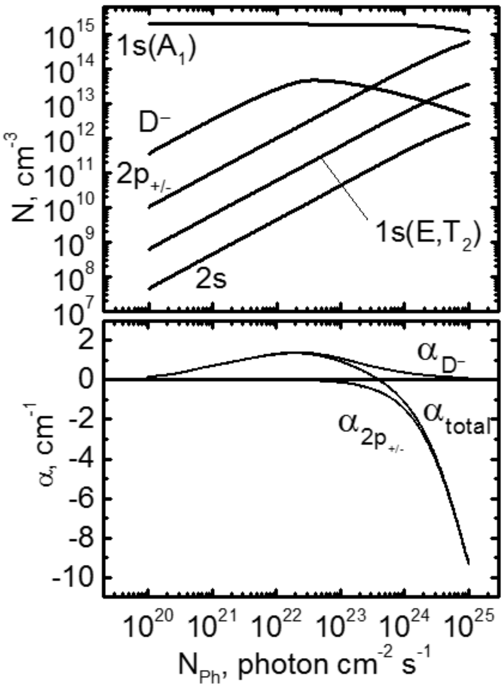

Fig. (5) The populations of donor states (upper graph) and absorption/amplification coefficient (lower graph) of Si:Bi calculated in the frame of intravalley approximation for 3×10^{15}cm^{-3} and compensation 0.1 versus 10.6 µm photon flux density N_{Ph}

Thus a four-level laser scheme can be realized from Bi donor transitions. The larger gain is expected on transitions from the $2p_{\pm}$ to the $1s(E)$ and $1s(T_2)$ states (Fig. 1). Calculations of the level populations and gain made using probability technique are presented on the *Figure 5*. The transition rates were estimated within the frame of the hydrogen-like centre model for D^0 centre states [20] and the zero-radius potential model for D^- centre states (neutral centre with an extra electron [18]). The lasing threshold value in Si:Bi (10^{24} photons×cm^{-2}×s^{-1}) is higher than that in Si:P due to the difference of the lifetimes of the $2p_{\pm}$ and $2p_0$ states.

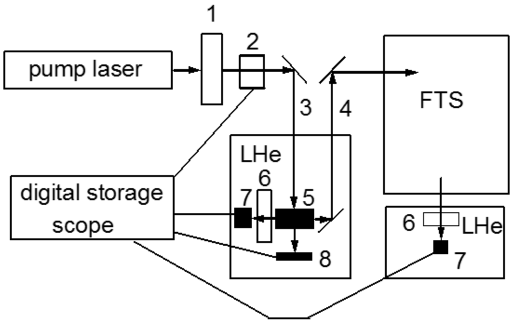

Fig. (6) Experimental setup: (1) attenuator, (2) CO_2 drag detector, (3) pump beam, (4) silicon emission beam, (5) silicon sample, (6) THz filter, (7) and (8) Ge detectors

3. Experiment

Low compensated (K< 0.01) Si:P, Si:Sb and Si:Bi samples were grown by the float zone procedure with simultaneous incorporation of the doping elements from the melt. The dominant donor concentrations in these samples are in the range of $(0.1\text{-}12)\times10^{15}$ cm^{-3}. Additionally, the Si:P crystals with $K \leq 0.3$ were prepared by neutron transmutation doping [21]. Samples with different doping concentrations were cut in form of rectangular parallelepipeds (typical crystal dimensions are $7\times7\times5$ mm^3) from the Si ingot and then polished to provide a high-*Q* resonator on internal reflection modes. The Si samples with the low doping concentration (ca. 10^{14} cm^{-3}) were used to identify the dominant impurity as well as the concentration of the incorporated electrically active centres by absorption spectroscopy.

The samples were mounted in a holder, which was immersed in a liquid helium (LHe) vessel (Fig. 6). A grating tunable TEA CO_2 laser with a peak output power up to 1.6 MW in the wavelength range 9.2-10.7 µm was used as the pump source. The THz emission from the optically pumped samples was registered by a LHe cooled Ge:Ga photodetector inside the same vessel. To prevent irradiation of the detector by the CO_2 laser, 1 mm thick sapphire filters were placed in front of the detectors. The pulses were recorded by the 500 MHz - bandwidth digital storage scope. For the spectral measurements the THz emission was guided by a stainless steel lightpipe into a Fourier transform spectrometre (FTS) and focused onto another LHe cooled Ge:Ga detector inside a separate cryostat. The spectrometre had a step-scan control, allowing to average the emission signal over the defined number of pulses.

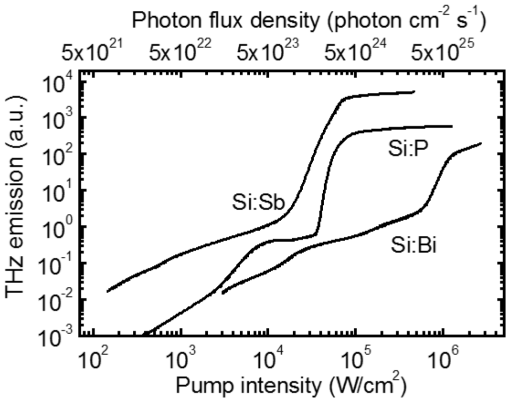

Fig. (7) The dependency of THz emission from silicon doped by different impurities

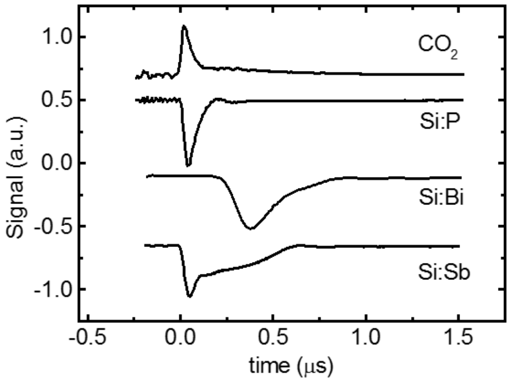

Fig. (8) The stimulated emission pulses from silicon doped by different impurities (negative signals) and CO_2 laser pulse (positive signal)

Spontaneous emission was detected with the Ge:Ga detector for various pump wavelengths from the silicon doped by phosphorus, antimony and bismuth. A linear dependence of the spontaneous emission signal on the pump photon flux density up to 6×10^{23} cm^{-2}s^{-1} was found.

All Si:P samples doped higher than 5×10^{14} cm^{-3} showed spontaneous emission when pumped by a CO_2 laser. The spontaneous emission increases with increasing doping concentration. For these samples stimulated emission was observed for doping concentration in the range $(0.8\text{-}5)\times10^{15}$ cm^{-3}. The neutron transmutation doped samples, which are heavily compensated, have some significant differences. First of all, the spontaneous emission is significantly higher than for the uncompensated samples provided by the same pump intensity. Secondly, the heavily compensated samples have lower laser thresholds. The CO_2 laser pump intensity, necessary to exceed the Si:P laser threshold for the 7 mm long sample from the best material, was about of 30 kW/cm^2 [11-13] at 10.6 μm line of the CO_2 laser (Fig. 7). The THz emission pulse from the Si:P laser started together with the pump pulse and had a duration of 70-100 ns, comparable with a full width of half maximum of the pump laser pulse (Fig. 8). The spectrum of the stimulated emission from the Si:P sample was measured by the FTS with a resolution of 0.2 cm^{-1} (Fig. 9). A line at 54.1 µm was recorded, which corresponds to the $2p_0\rightarrow1s(T_2)$ intracentre transition.

Stimulated emission from Si:Sb has been observed for the pump photon flux density higher than 10^{24} photons×cm^{-2}×s^{-1} (20 kW×cm^{-2}) for the 9.6 μm pump line (Fig. 7). Pumping by a line from the 10 μm band of CO_2 laser emission band requires a factor of 1.5-2 higher photon flux density to reach the laser threshold. This difference is caused by the different lattice absorption of the pump emission: 0.3 cm^{-1} and 1.1 cm^{-1} for 9.6 μm and 10.6 μm pump lines correspondingly [15]. The pulse shapes of the pump laser and the THz Si:Sb laser are presented in Fig. (8). The Si:Sb stimulated emission spectrum was measured by the FTS with a resolution of 0.2 cm^{-1} (Fig. 9). The spectrum consists of a single line at 171.8 cm^{-1} (5.15 THz or 58.2 μm). The interesting feature of the Si:Sb in comparison with the Si:P laser is that it ends on the $1s(T_2{:}\Gamma_8)$ quadruplet state. The spin-orbit coupling splits the $1s(T_2)$ state into the doublet $1s(T_2{:}\Gamma_7)$ and quadruplet $1s(T_2{:}\Gamma_8)$, separated with 0.3 meV energy spacing,, since Sb has a higher atomic number than that of P impurity centres.

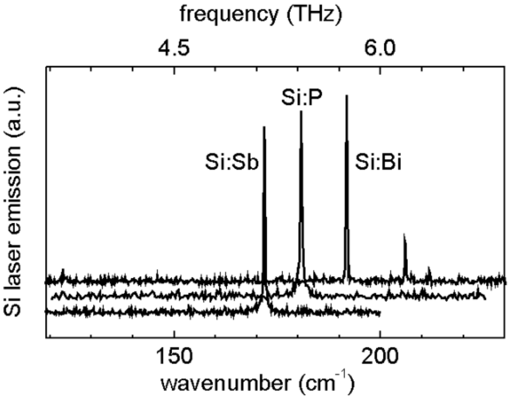

Fig. (9) The spectra of stimulated emission from silicon doped by different impurities

In the Si:Bi samples a stimulated emission effect was observed for doping concentration in the range of $N_{Bi}=(6\text{-}12)\times10^{15}$ cm^{-3}. The CO_2 laser pump threshold intensity for Si:Bi lasing was 100-300 kW×cm^{-2} at the pump wavelength of 9.6 µm (photon flux density of $(5\text{-}15)\times10^{25}$ quantum×cm^{-2}×s^{-1}) [13,14]. Pumping by a line from the 10 µm band of the CO_2 laser required a factor ~2 higher power and exhibits the lower output signal and the longer delay of the lasing pulse. The stimulated emission pulse appears always with an essential time delay, 50-200 ns, (Fig. 8) after the peak of the pump laser pulse, while the spontaneous emission has no such a delay for all pump frequencies. Two strong emission lines, having the relatively low laser thresholds, and corresponding the $2p_{\pm}\rightarrow\{1s(E),\ 1s(T_2{:}\Gamma_8)\}$ transitions were registered in the Si:Bi spectra under the pumping by of the CO_2 laser (Fig. 9).

3. Conclusion

The influence of the nonequilibrium phonons on the populations of the working states in Si:Bi appear due to the bottled-neck effect in the decay of TA ($\approx$ 20 meV) acoustic phonons. Additionally, it should be pointed out that the times of life of the $1s(E)$, $1s(T_2)$ laser states have been estimated in the simplified model using hydrogen-like eigenfunctions. This has to be defined more exactly. Also it is important to take into account the possibility of the reabsorption on the $2p_0 \rightarrow 1s(A_1)$ transition of the emitted TO intervalley optical phonons by Bi centres before they decay into the acoustic phonons. The latter can increase the time of life of the $2p_0$ state. The frequency coverage might be extended also by using other dopants such as As and Li. Si lasers covering 5-6 THz region with a tunability of about 1% are expected to be feasible.

References

[1] A.A. Andronov et al., “Amplification of Far-Infrared Radiation in Germanium During the Population Inversion of Hot Holes”, JETP. Lett., 30 (1979) 551-555.

[2] L.S. Mazov and I.M. Nefedov, “Numerical Computation of Holes Population Inversion and FIR Amplification in Silicon”, in A.A. Andronov (eds) Submillimeter Wave Lasers in Semiconductors Using Hot Holes, IAP AS, Gorky, (1986) pp. 153-166.

[3] A.V. Muravjov et al., “Amplification of Far-Infrared Radiation on Light Hole Cyclotron Resonance in Silicon in Crossed Electric and Magnetic Fields”, in M. von Ortenberg and H.-U. Müller (eds) Proc. of 21th Int. Conf. on Infrared and Millimeter Waves, Berlin, CTh11 (1996).

[4] A.V. Muravjov et al., “Population Inversion of Landau Levels in the Valence Band in Crossed Electric and Magnetic Fields”, phys. stat. sol. (b), 205 (1998) 575-585.

[5] A.A. Andronov et al., “Stimulated Emission in the Long-Wavelength IR Region from Hot Holes in Ge in Crossed Electric and Magnetic Fields”, JETP. Lett., 40 (1984) 804-806.

[6] Y.L. Ivanov, “Generation of Cyclotron Radiation by Light Holes in Germanium”, Opt. Quant. Elect., 23 (1991) S253-S265.

[7] V.N. Shastin, “Far-Infrared Active Media Based on Inraband and Shallow Impurity States Transitions in Si”, in M. von Ortenberg and H.-U. Müller (eds) Proc. of 21th Int. Conf. on Infrared and Millimeter Waves, Berlin, CT2 (1996).

[8] E.E. Orlova and V.N. Shastin, “Inverse Population of Bismuth Donor Excited States and FIR Amplification in Silicon Under of Optical in Si”, in M. von Ortenberg and H.-U. Müller (eds) Proc. of 21th Int. Conf. on Infrared and Millimeter Waves, Berlin, CTh4 (1996).

[9] E.E. Orlova, “Nonequilibrium Population of Shallow Impurity States in Semiconductors and Amplification of Far-Infrared Radiation”, Ph.D. thesis, Institute for Physics of Microstructures RAS, Nizhny Novgorod, 128 Pages (2002).

[10] E.E. Orlova, “Longliving shallow donor states in silicon-life time calculation”, in J.H. Davies and A.R. Long (eds) Proc. of 26th Int. Conf. on the Physics of Semiconductors, 29 July-2 August (2002), Cambridge, 3, p. 123.

[11] S.G. Pavlov et al., “Stimulated emission from donor transitions in silicon”, Phys. Rev. Lett., 84 (2000) 5220-5223.

[12] T.O. Klaassen et al., “The emission spectra of optically pumped Si-based THz lasers”, in M. Chamberlain et. al (eds) Proc. of 2002 IEEE Tenth Int. Conf. on Terahertz Electronics, (2002) pp. 89-90.

[13] H.-W. Hübers et al., “Terahertz emission spectra of optically pumped silicon lasers”, phys. Stat. sol. (b), 233 (2002) 191-196.

[14] S.G. Pavlov et al., “Far-infrared stimulated emission from optically excited bismuth donors in silicon”, Appl. Phys. Lett., 80 (2002) 4717-4719.

[15] S.G. Pavlov et al., “Terahertz optically pumped Si:Sb laser”, J. Appl. Phys., 92 (2002) 5632.

[16] A.K. Ramdas and S. Rodriguez, “Spectroscopy of the solid-state analogues of the hydrogen atom: donors and acceptors in semiconductors”, Reports on Prog. in Phys., 44 (1981) 1297-1387.

[17] T.G. Castner, “Raman spin-lattice relaxation of shallow donors in silicon”, Phys. Rev., 130 (1963) 58-75.

[18] E.M. Gershenzon, A.P. Mel’nikov and R.I. Rabinovich, “H^- like impurity centers, molecular complexes and electron delocalization in semiconductors”, in A.L. Efros and M. Pollak (eds.) *Electron-Electron Interactions in Disordered Systems*, Elsevier Science Publishers, Amsterdam, (1985) pp. 483-554.

[19] N.R. Battler, P. Fisher and A.K. Ramdas, “Excitation spectrum of bismuth donors in silicon”, Phys. Rev. B, **12** (1975) 3200-3209.

[20] V.N. Abakumov, V.I. Perel and I.N. Yassievich, **“Nonradiative Recombination in Semiconductors”**, North-Holland Publ. Co. (Oxford, 1991).

[21] I.M. Gres'kov et al., “Influence of growth defects on the electrical properties of radiation-doped silicon”, Sov. Phys. – Semicond., 12 (1978) 1118-1120.

IRAQI JOURNAL OF APPLIED PHYSICS
Vol. 16, No.3, July-September 2020, pp. 27-32

Heterojunction Solar Cell Based on Highly-Pure Nanopowders Prepared by DC Reactive Magnetron Sputtering

Saja H. Faisal
Mohammed A. Hameed

Department of Physics,
College of Science,
University of Baghdad,
Baghdad, IRAQ

In this work, a novel design for the NiO/TiO$_2$ heterojunction solar cells is presented. Highly-pure nanopowders prepared by dc reactive magnetron sputtering technique were used to form the heterojunctions. The electrical characteristics of the proposed design were compared to those of a conventional thin film heterojunction design prepared by the same technique. A higher efficiency of 300% was achieved by the proposed design. This attempt can be considered as the first to fabricate solar cells from highly-pure nanopowders of two different semiconductors.

Keywords: Heterojunctions; Optoelectronics; Magnetron sputtering; Nanopowder
Received: 12 August 2020; **Revised:** 26 August 2020; **Accepted:** 2 September 2020

1. Introduction

Search for new designs and configurations of solar cells still a hot topic in light of the reality of alternative and renewable energy over world. Researchers are hard working to reach higher efficiencies as well as to find new materials with better optoelectronic properties. Nanomaterials can be excellent candidates for these purposes due to their advantages when compared to the bulk materials [1-3]. The drastic increase in the number of particles at the nanoscale with respect to thin films can successfully contribute to enhance the efficiency of the optoelectronic device [4-6].

When two different semiconducting nanomaterials (such as TiO$_2$ and NiO) are mixed in the powder form, a large number of junctions can be formed within the mixture. If these materials are different in their conductivities (n- and p-type), then a heterojunction can be formed as one n-type particle is in contact to one p-type particle, as shown in Fig. (1a). Therefore, the high density of nanoparticles can absorb higher amount of the incident radiation and then produce higher current density [7,8]. Roughly, the current density produced by nanopowder heterojunctions can be higher than that produced by corresponding thin film heterojunctions by three orders of magnitude [9,10]. The research interest in NiO/TiO$_2$ heterojunction is increasing due to its distinguished features serving many photonic and optoelectronic applications [11-16].

The nanopowders may play their own roles away from the different others since the radiation is incident on both sides of the heterojunction as well as on the junction region, as shown in Fig. (1b). Also, not all nanoparticles get in contact with others of different type as the contact is fundamentally a mechanical process [17-22]. Such roles may support the main process of converting the incident light into electrical current. For example, TiO$_2$ nanoparticles may act as photocatalysts [23-28], while NiO nanoparticles may store the absorbed energy in the UV region and then emit it in the visible region [29-36].

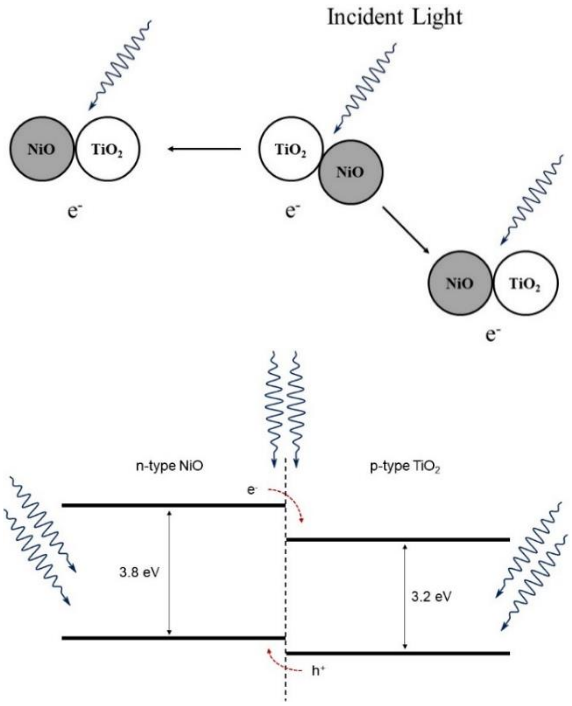

Fig. (1) Principle of nanopowder heterojunction formation (upper) and energy band diagram of such heterojunction (lower)

In this work, highly-pure titanium dioxide and nickel oxide nanopowders were mixed and spread over the surface of a nonmetallic substrate to fabricate solar cell device. These nanopowders were prepared by dc reactive magnetron sputtering.

2. Experimental Part

A homemade dc reactive magnetron sputtering system was used to deposit metal oxide thin films. Highly-pure titanium and nickel (99.99%) targets were sputtered in existence of oxygen to deposit titanium dioxide (TiO_2) and nickel oxide (NiO) thin films on glass substrates. Details of the preparation conditions can be found elsewhere [37-40]. The nanopowders were extracted from thin film samples by conjunctional freezing-assisted ultrasonic extraction method [41,42].

The structural characteristics of the prepared thin films were determined by x-ray diffraction (XRD), scanning electron microscopy (SEM), and energy-dispersive x-ray spectroscopy (EDS), while their the spectroscopic characteristics were determined by the Fourier-transform infrared (FTIR) and UV-visible spectroscopy.

The nanopowders were mixed, immersed in a transparent solution and spread over nonmetallic substrates. The mixture was covered with a glass to allow the incident radiation to reach the nanopowder mixture. Figure (2) shows the proposed design and photograph of solar cell device proposed in this work.

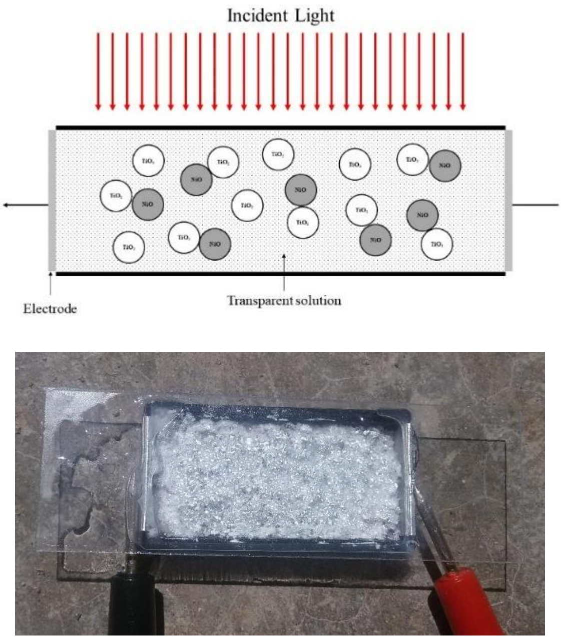

Fig. (2) Proposed design and photograph of nanopowder heterojunction solar cell

3. Results and Discussion

Figure (3) shows the XRD patterns of TiO_2 and NiO thin films prepared in this work. It is clear that both samples exhibit high structural purity as no peaks belonging to other materials than TiO_2 or NiO are observed. In TiO_2 samples, both phases (rutile; R and anatase; A) are recognized [43], however, the anatase phase is apparently dominant as the crystal planes belonging to anatase TiO_2 are more than those belonging to rutile TiO_2. Such dominance (~70% anatase and ~30% rutile) can be precisely determined by [44]:

$$f = \frac{1}{1+1.26\frac{I_A}{I_R}} \qquad (1)$$

where I_A/I_R is the ratio of the intensity of anatase to the intensity of rutile as determined from the x-ray pattern

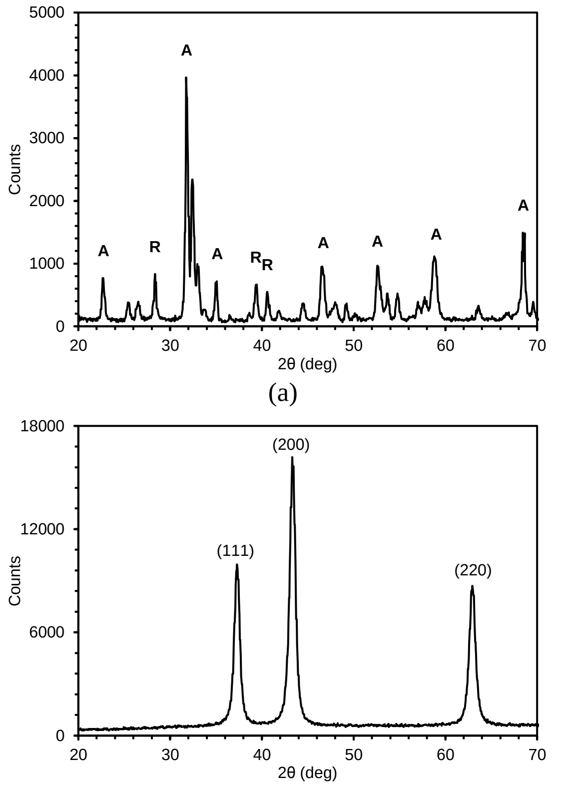

(a)

(b)

Fig. (3) XRD patterns of (a) TiO_2 and (b) NiO thin films prepared in this work

The XRD pattern of the prepared NiO thin film exhibits only three peaks belonging to (111), (200) and (220) crystal planes [45,46].

Figure (4) shows the 3D AFM images of both samples prepared and mixed in this work. The formation of nanostructures is confirmed with peak-to-peak roughness of 20.66 and 4.39 nm for TiO_2 and NiO samples, respectively. Such values of roughness ensures extremely wide surfaces to receive the incident radiation, which reasonably increase the input power required for higher efficiency of such optoelectronic converters.

Further confirmation of the structural purity of the prepared samples can be presented by the FTIR results shown in Fig. (5). The main peaks belonging to the vibration of Ti-O, O-Ti-O and Ni-O are observed with additional peaks belonging to the O-H group, which are resulted from the exposure to the environment [47-50]. Therefore, both samples can be described as highly-pure. This would support the assumption that the whole interaction with the incident radiation is performed by TiO_2 and NiO nanoparticles as well as the heterojunctions formed from them.

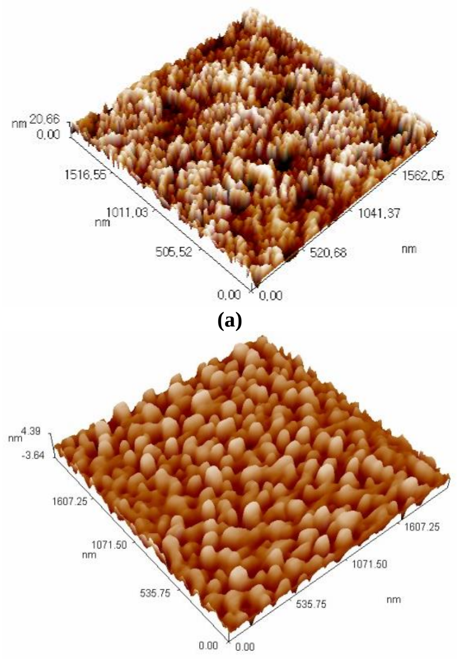

(a)

(b)

Fig. (4) AFM 3D images of (a) TiO_2 and (b) NiO thin films prepared in this work

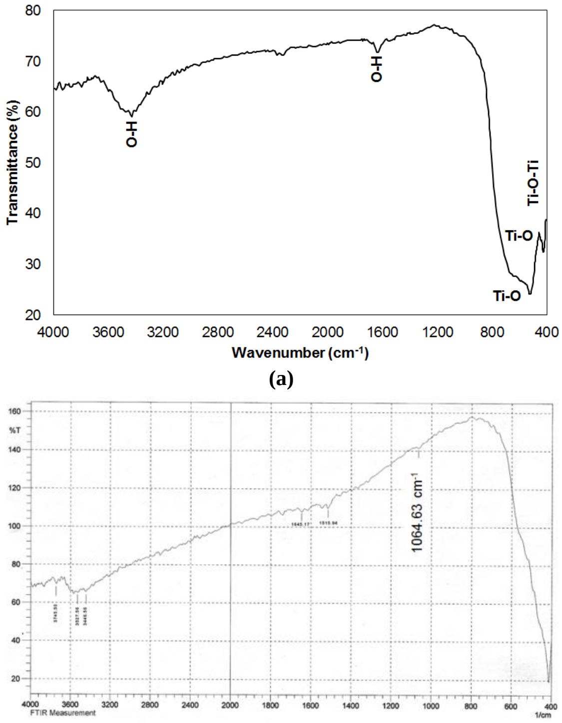

(a)

(b)

Fig. (5) FTIR spectra of (a) TiO_2 and (b) NiO thin films prepared in this work

Figure (6) shows the absorption spectra of TiO_2 and NiO thin films prepared in this work. It is apparent that the NiO films absorb higher than TiO_2 films especially in the UV region. The energy band gap (E_g) can be determined for both TiO_2 and NiO samples to be 3.85 and 3.2 eV, respectively, which is in good agreement to the typical values (see Fig. 1b) [51]. In the conventional p-n heterojunction solar cell design, the solar radiation is incident on the p-type side (NiO). Therefore, the main expected losses are attributed to lattice thermalization, transparency, recombination, junction, and contact voltage [2]. In the proposed design, most of these losses are minimized while some are omitted (transparency). Accordingly, the absorption and conversion efficiencies are increased. This assumption should be confirmed by the comparison of electrical characteristics of the proposed design to the conventional thin film design prepared by the same technique.

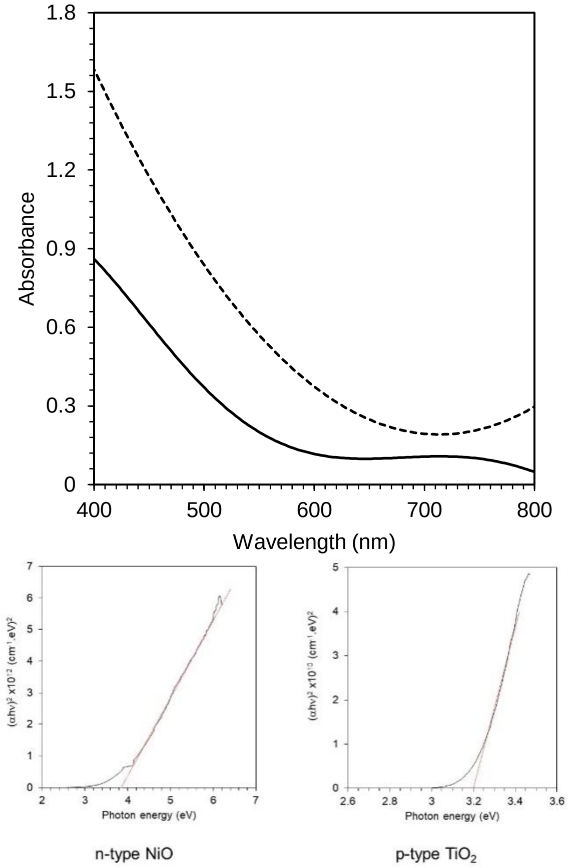

Fig. (6) Absorption spectra and energy band gap of the prepared TiO_2 and NiO thin films

Figure (7) shows the current-voltage characteristics of the thin film heterojunction solar cell (7a) and nanopowder heterojunction solar cell proposed in this work (7b). At constant incident solar power density of 100 mW/cm^2, the thin film device shows a quantum efficiency of 7.64% while the nanopowder device shows a quantum efficiency of 23.11%. With three times higher efficiency, the advantage of the proposed design is obviously recognized.

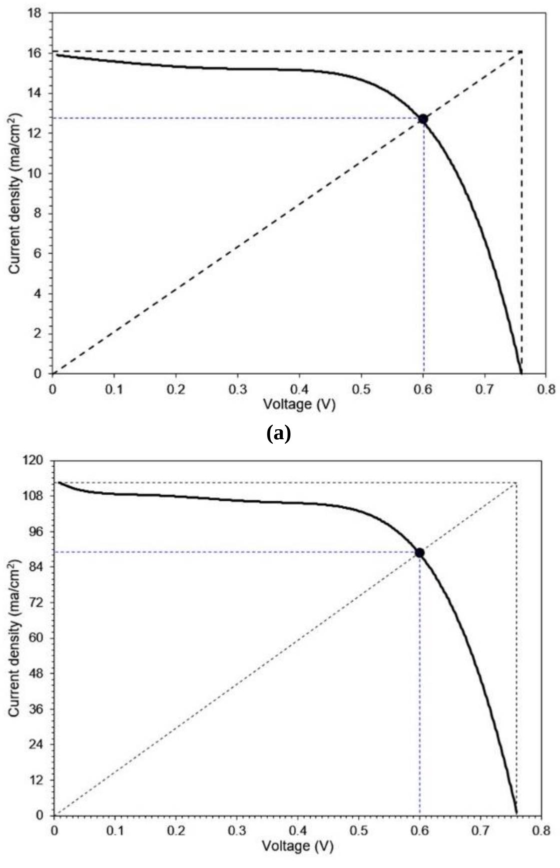

(a)

(b)

Fig. (7) I-V characteristics of (a) thin film heterojunction and (b) nanopowder heterojunction solar cells prepared in this work

4. Conclusions

In concluding remarks, a novel design for the NiO/TiO$_2$ heterojunction solar cells is presented. Highly-pure nanopowders prepared by dc reactive magnetron sputtering technique were used to form the heterojunctions. The electrical characteristics of the proposed design were compared to those of a conventional thin film heterojunction design prepared by the same technique. A higher quantum efficiency of 300% was achieved by the proposed design. According to the available resources, this attempt can be considered as the first to fabricate solar cells from highly-pure nanopowders of two different semiconductors.

References

[1] M.C. Gupta and J. Ballato (editors), “The Handbook of Photonics”, 2nd ed., CRC Press, Taylor & Francis Group (FL), Ch. 8, 1-27 (2007).

[2] M. Grundmann, “The Physics of Semiconductors”, 3rd ed., Springer (Cham), 461-487 (2016)

[3] S.K. Kulkarni, “Nanotechnology: Principles and Practices”, 3rd ed., Springer (Cham), p. 295 (2015).

[4] B. Bhushan (Ed.), “Springer Handbook of Nanotechnology”, Springer, p. 27, 151, 438 (2004).

[5] M.A. Behnajady, N. Modirshahla, M. Shokri, H. Elham and A. Zeininezhad, “The effect of particle size and crystal structure of titanium dioxide nanoparticles on the photocatalytic properties", J. Environ. Sci. Health Part A, 43, 460-467 (2008).

[6] S. Anandan, Y. Ikuma and K. Niwa, “An Overview of Semi-Conductor Photocatalysis: Modification of TiO$_2$ Nanomaterials”, Solid State Phenom., 162, 239-260 (2010).

[7] O.A. Hamadi, B.A.M. Bader and A.K. Yousif, “Electrical Characteristics of Silicon p-n Junction Solar Cells Produced by Plasma-Assisted Matrix EtchingTechnique”, J. Eng. Technol., 26(8), 995-1001 (2008).

[8] K.O. Ukoba, F.L. Inambao and A.C. Eloka-Eboka, “Fabrication of Affordable and Sustainable Solar Cells Using NiO/TiO$_2$ P-N Heterojunction”, Int. J. Photoenergy, Vol. 2018, Article ID 6062390, DOI: 10.1155/2018/6062390

[9] L.C. Sim, K.W. Ng, S. Ibrahim and P. Saravanan, “Preparation of Improved p-n Junction NiO/TiO$_2$ Nanotubes for Solar-Energy-Driven Light Photocatalysis”, Int. J. Photoenergy, Vol. 2013, Article ID 659013, DOI: 10.1155/2013/659013

[10] Z.H. Ibupoto, M.A. Abbasi, X. Liu, M. S. AlSalhi and M. Willander, “The Synthesis of NiO/TiO$_2$Heterostructures and Their Valence Band Offset Determination”, J. Nanomater., Vol. 2014, Article ID 928658, DOI: 10.1155/2014/928658

[11] G. Zhang, X. Tang, X. Chen and W. Zha, “The Effects of the Content of NiO on the Microstructure and Photocatalytic Activity of the NiO/TiO$_2$ Composite Film”, Mater. Sci., 24(4), 372-75 (2018).

[12] X. Yu, J. Zhang, Z. Zhao, W. Guo, J. Qiu, X. Mou, A. Li, J.P. Claverie and H. Liu, “NiO–TiO$_2$ p–n heterostructured nanocables bridged by zero-band gap rGO for highly efficient photocatalytic water splitting”, Nano Energy, 16, 207-217 (2015).

[13] K.O. Ukoba and F.L. Inambao, “Study of Optoelectronic Properties of Nanostructured TiO$_2$/NiO Heterojunction Solar Cells”, Proc. World Cong. on Eng. Comp. Sci. 2018, Vol I (WCECS 2018), October 23-25, 2018, San Francisco, USA.

[14] K.O. Ukoba and F.L. Inambao, “Modeling of Fabricated NiO/TiO$_2$ P-N Heterojunction Solar Cells”, Int. J. Appl. Eng. Res., 13(11), 9701-9705 (2018).

[15] J.-Z. Chen, T.-H. Chen, L.-W. Lai, P.-Y. Li, H.-W. Liu, Y.-Y. Hong and D.-S. Liu, “Preparation and Characterization of Surface Photocatalytic Activity with NiO/TiO_2 Nanocomposite Structure”, Materials, 8, 4273-4286 (2015).

[16] J. Cui, S. Chen, H. Liu and Z. Huang, “Nano-p–n junction heterostructures enhanced TiO_2nanobeltsbiosensingelectrode”, J. Solid State Electrochem., 18, 2693-2699 (2014).

[17] U. Diebold, “The surface science of titanium dioxide”, Surf. Sci. Rep., 48(5-8), 53-229 (2003).

[18] S.M. Gupta and M. Tripathi, “A review of TiO_2 nanoparticles”, Chinese Sci. Bull., 16, 1639-1657 (2011).

[19] A.T. Baxton and L. Thien-Nga, “Electronic structure of reduced titanium dioxide”, Phys. Rev. B, 57, 1579-1584 (1998).

[20] J. Jia, H. Yamamoto, T. Okajima and Y. Shigesato, “On the Crystal Structural Control of Sputtered TiO_2 Thin Films”, Nanoscale Res Lett., 11(1), 324 (2016).

[21] Y. Zhao, C. Li, X, Liu, F. Gu, H. Jiang, W. Shao, L. Zhang and Y. He, “Synthesis and Optical Properties of TiO_2 Nanoparticles”, Mater. Lett., 61(1), 79-83 (2007).

[22] A. Molea and V. Popescu, “The obtaining of Titanium dioxide nanocrystalline powders”, Optoelectron. Adv. Mater., 5(3), 242-246 (2011).

[23] E.A. Al-Oubidy and F.J. Al-Maliki, “Photocatalytic activity of anatase titanium dioxide nanostructures prepared by reactive magnetron sputtering technique”, Opt. Quantum Electron., 51(1), 23 (2019).

[24] O.A. Hammadi, F.J. Kadhim and E.A. Al-Oubidy, “Photocatalytic Activity of Nitrogen-Doped Titanium Dioxide Nanostructures Synthesized by DC Reactive Magnetron Sputtering Technique”, Nonl. Opt. Quantum Opt., 51(1-2), 67-78 (2019).

[25] M. Kanna and S. Wongnawa, “Mixed Amorphous and Nanocrystalline TiO_2Powders Prepared by Sol-Gel Method: Characterization and Photocatalytic Study”, Mater. Chem. Phys., 110, 166-175 (2008).

[26] J.Y. Park, C. Lee, K.W. Jung and D. Jung, “Structure related photocatalytic properties of TiO_2”, Bull. Korean Chem. Soc., 30, 402-404 (2009).

[27] A Fujishima, X. Zhang, D. Tryk, “TiO_2photocatalysis and related surface phenomena”, Surf. Sci. Rep., 63(12), 515-582 (2008).

[28] W.J. Yang, C.Y. Hsu, Y.W. Liu, R.Q. Hsu, T.W. Lu, C.C. Hu, “The structure and photocatalytic activity of TiO_2 thin films deposited by dc magnetron sputtering”, Superlatt. Microstruct., 52, 1131-1142 (2012).

[29] H. Sato, T. Minami, S. Takata and T. Yamada, “Transparent conducting p-type NiO thin films prepared by magnetron sputtering”, Thin Solid Films, 236, 27-31 (1993).

[30] R. CercKorošec and P. Bukovec, “Sol-Gel Prepared NiO Thin Films for Electrochromic Applications”, Acta Chim. Slov., 53, 136-147 (2006).

[31] P.S. Patil and L.D. Kadam, “Preparation and characterization of spray pyrolyzed nickel oxide (NiO) thin films”, Appl. Surf. Sci., 199, 211-221 (2002).

[32] F.I. Ezema A.B.C Ekwealor and R.U. Osuji, “Optical properties of chemical bath deposited nickel oxide (NiO_x) thin films”, Superficies y Vacío, 21(1), 6-10 (2008).

[33] A.R. Balu, “Nanocrystalline NiO thin films prepared by a low cost simplified spray technique using perfume atomizer”, J. Electron Dev., 13, 920-930 (2012).

[34] H.-L. Chen, Y.-M. Lu and W.-S. Hwang, “Effect of Film Thickness on Structural and Electrical Properties of Sputter-Deposited Nickel Oxide Films”, Mater. Trans., 46(4), 872-879 (2005).

[35] M. Guziewicz, “Electrical and optical properties of NiO films deposited by magnetron sputtering”, Optica Applicata, XLI(2), 431-440 (2011).

[36] Y. Ashok Kumar Reddy, B. Ajitha and P. Sreedhara Reddy, “Influence of Growth Temperature on the Properties of DC Reactive Magnetron Sputtered NiO Thin Films”, Int. J. of Current Eng. and Technol., Special issue, 351-357 (2014).

[37] O.A. Hammadi, M.K. Khalaf and F.J. Kadhim, “Fabrication of UV Photodetector from Nickel Oxide Nanoparticles Deposited on Silicon Substrate by Closed-Field Unbalanced Dual Magnetron Sputtering Techniques”, Opt. Quantum Electron., 47(12), 3805-3813 (2015).

[38] E.A. Al-Oubidy and F.J. Al-Maliki, “Effect of Gas Mixing Ratio on Energy Band Gap of Mixed-Phase Titanium Dioxide Nanostructures Prepared by Reactive Magnetron Sputtering Technique”, Iraqi J. Appl. Phys., 14(4), 19-23 (2018).

[39] F.J. Al-Maliki, O.A. Hammadi and E.A. Al-Oubidy, “Optimization of Rutile/Anatase Ratio in Titanium Dioxide Nanostructures prepared by DC Magnetron Sputtering Technique”, Iraqi J. Sci., 60 (Special Issue), 91-98 (2019).

[40] F.J. Al-Maliki and E.A. Al-Oubidy, “Effect of gas mixing ratio on structural characteristics of titanium dioxide nanostructures synthesized by DC reactive magnetron sputtering”, Physica B: Cond. Matter, 555, 18-20 (2019).

[41] O.A. Hammadi, “Production of Nanopowders from Physical Vapor Deposited Films on Nonmetallic Substrates by Conjunctional

Freezing-Assisted Ultrasonic Extraction Method", Proc. IMechE, Part N, J. Nanomater. Nanoeng. Nanosys., 232(4), 135-140 (2018).

[42] O.A. Hammadi, "Effects of Extraction Parameters on Particle Size of Titanium Dioxide Nanopowders Prepared by Physical Vapor Deposition Technique", Plasmonics, 15 (2020),DOI: 10.1007/s11468-020-01205-8

[43] M. Ladd and R. Palmer, "Structure Determination by X-Ray Crystallography", 5th ed., Springer (NY), p. 568 (2013).

[44] S.F. Bertram, "Handbook of X-rays", ed. E.F. Kaelbe, McGraw-Hill (NY), p. 817 (1976).

[45] JCPDS 1972, 22-1189, Joint Committee on Powder Standards, Italy (1972).

[46] M. Awais, "Deposition and characterization of NiO_x coatings by magnetron sputtering", Surf. Coat. Technol., 204(16-17), 2729-2739 (2010).

[47] N.N. Greenwood and E.J.F. Ross, "Index of Vibrational Spectra of Inorganic and Organometallic Compounds", vol. I, Butterworth Group (London), p. 326, 328 (1960).

[48] N.N. Greenwood and E.J.F. Ross, "Index of Vibrational Spectra of Inorganic and Organometallic Compounds", vol. II, Butterworth Group (London), p. 457 (1963).

[49] N.N. Greenwood and E.J.F. Ross, "Index of Vibrational Spectra of Inorganic and Organometallic Compounds", vol. III, Butterworth Group (London), p. 800, 1078 (1966).

[50] V.P. Tolstoy, I.V. Chernyshova and V.A. Skryshevsky, "Handbook of Infrared Spectroscopy of Ultrathin Films", John Wiley & Sons, Inc. (NJ), p. 435 (2003).

[51] P.M. Martin, "Handbook of Thin Film Deposition Techniques", Elsevier, p. 4 (2010).

IRAQI JOURNAL OF APPLIED PHYSICS
Vol. 16, No. 3, July-September 2020, pp. 33-38

Energy Transfer Calculations Based on Fluorescence Spectra of Acriflavine and Rhodamine B Laser Dyes

Qusay R. Ali [1]
Bahaa T. Chiad [2]
Abbas J. Al-Wattar [2]

[1] *Department of Physics, College of Science, University of Baghdad, Baghdad, IRAQ*
[2] *Department of Physics, College of Science, University of Baghdad, Baghdad, IRAQ*

In this work, the fluorescence spectra of a mixture of two laser dyes; acriflavine and rhodamine B in different solvents; ethanol and DMSO, were recorded and studied. The energy transfer efficiency of the prepared samples was determined and studied by comparing some parameters such as the critical transfer distance, the emission lifetime, and the rate constant for energy transfer at different concentrations of these solutions. The emission lifetime of the dye mixture in DMSO was shorter than that in ethanol by 35.6%.

Keywords: Laser dyes; Energy transfer; Fluorescence; Rhodamine B; Acriflavine
Received: 5 June 2020; **Revised:** 28 July 2020; **Accepted:** 4 August 2020

1. Introduction

Fluorescence energy transfer is the transfer of the excited state energy from a donor (D) to an acceptor (A) [1]. This transfer occurs without the appearance of photon and is primarily a result of dipole–dipole interaction between the donor and the acceptor. The rate of energy transfer depends upon the extent of overlap of the emission spectrum of the donor with the absorption spectrum of the acceptor, the relative orientation of the donor and acceptor transition dipoles and the distance between these molecules [2]. The nonradiative energy transfer occurs as a result of dipole–dipole coupling between the donor and the acceptor, and does not involve the emission and reabsorption of photons. The other process is radiative process, which depends upon other properties of the sample, such as size of the sample, container, optical densities of the sample at the excitation and emission wavelengths and the precise geometric arrangements of the excitation and emission axes [3].

In contrast to these trivial factors nonradiative energy transfer depends upon the molecular details of donor–acceptor pairs. It is important to note here that the phenomenon of energy transfer also contains molecular information, which is different from revealed by other phenomena such as solvent relaxation, excited state reactions, and fluorescence quenching or fluorescence polarization. These other spectral properties of fluorescence reveal primarily the interactions with the other molecules in the surrounding solvent shell. The important parameter for energy transfer that nonradiative energy transfer is effective over distance ranging of 50Å. The intervening of solvent or other macromolecules has little effect on the efficiency of the energy transfer, which depends primarily on the D–A distances [4].

So, briefly the transfer of electronic energy from one molecule to another generally occurs in one of the following two ways.

1- Radiative energy transfer mechanism [5].
2- Non-Radiative energy transfer mechanism: which includes
a- Resonance energy transfer [6].
b- collision energy transfer [7].

Energy transfer in a mixture of dyes have been established as an effective mechanism for extending the wavelength of lasing, tenability, enhancement of power of the dye laser and low pump power requirement; dye lasers have some limitations as the dye solution used as an active medium absorbs energy from the excitation source in a very limited range and so the emission band also has these limitations. If a dye laser has to be used as an ideal source its spectral region needs to be extended. In order to extend the spectral region of operation mixtures of different dye solutions/dye molecules embedded in solid matrices are being used. The work on energy transfer between different dye molecules in such mixtures in various solvents and solid matrices is, therefore, of great importance. The use of such energy transfer in dye lasers is also helpful in minimizing the photo-quenching effects and thereby, increasing the laser efficiency [8,9].

The energy transfer is manifested by a quenching of donor emission, an increased emission of acceptor excited via the donor, a decrease in donor photobleaching rate, and a decrease in donor lifetime [10]. Figure (1) shows the energy level scheme of the resonant transitions of a donor- acceptor pair [11].

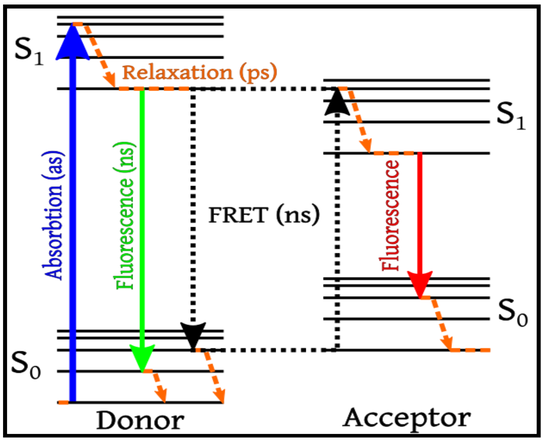

Fig. (1) Energy level scheme of the resonant transitions [11]

Forster has developed a theory for non-radiative energy transfer in terms of the resonance dipole-dipole interaction mechanism, and has shown that rate constant for dipole energy transfer K_{ET} between donor D and acceptor A, is given by

$$K_{ET} = 1.25 \times 10^{17} \frac{\phi_D}{n^4 \tau_D R^6} \int_0^\infty \frac{F_D(\upsilon)\epsilon_A(\upsilon)d\upsilon}{\upsilon^4} \qquad (1)$$

where ϕ_D is the quantum yield of donor emission, τ_D is the lifetime of the emission, n is the solvent refractive index and R is the distance in nm between D* and A, $F_D(\upsilon)$ is the emission spectrum of the donor, expressed in wave number and normalized to unity and $\varepsilon_A(\upsilon)$ is the molar excitation coefficient of A at the wave number υ [1].

The critical transfer distance (R_o) is generally used to indicate the strength of the interaction between donor and acceptor molecules and by definition, is the distance where the rate constant for energy transfer K_{ET} is equal to the rate constant for fluorescence by donor in the absence of acceptors $1/\tau$. Equation (1) can re-written as:

$$K_{ET} = \frac{1}{\tau_D}\left(\frac{R_o}{R}\right)^6 \qquad (2)$$

substituting Eq. (2) into Eq. (1) gives:

$$R_o^6 = 1.25 \times 10^{17} \frac{\phi_D}{n^4} \int_0^\infty \frac{F_D(\upsilon)\epsilon_A(\upsilon)d\upsilon}{\upsilon^4} \qquad (3)$$

The conditions favoring energy transfer are a large overlap between fluorescence spectrum of the donor and the absorption spectrum of acceptor, a large value of ε_A, and a large value of fluorescence quantum yield of donor.

$$\frac{\tau_D}{\tau} = 1 + \tau_D K_{AD}[A] \qquad (4)$$

when $\tau = 1/2\tau_M$, $[A]_h = [A]_{1/2}$: half-value concentration, which is given by

$$[A]_{1/2} = {}^{1}\!/_{K_{SV}} \qquad (5)$$

where

$$K_{SV} = \tau_D K_{AD} \qquad (6)$$

then the critical transfer distance between donor and acceptor is

$$R_o = \frac{7.35}{\sqrt[3]{[A]_{1/2}}} = 7.35(K_{SV})^{1/3} \qquad (7)$$

Resonance transfer is often the dominant mechanism of energy transfer in concentrated solutions and can occur over intermolecular distance of 10-100 Å **[12].**

2. Experimental Part

The solutions of acriflavine and rhodamine B dyes of primary concentration of 10^{-3} M were prepared by dissolving the appropriate amounts of these dyes (weighted by Mattler balance of 0.1mg sensitivity) in the solvents. The weight, W, of the dye (in gm) was calculated using the following equation:

$$W = M_w V[M]/1000 \qquad (8)$$

where M_w is the molecular weight of dye (gm/mole), V is the volume of the solvent (ml), and [M] is dye concentration (M= mole/l). The concentration of each dye was then diluted to get concentrations in the range of 10^{-3} M to 1×10^{-5} M according to:

$$[M_1]V_1 = [M_2]V_2 \qquad (9)$$

where, $[M_1]$ is the high concentration, V_1 is the volume before dilution, $[M_2]$ is the low concentration, and V_2 is the total volume after dilution.

The absorption spectra of the prepared samples were recorded using UV-VIS-NIR spectrophotometer (model UV-3600) in UM, covering the wavelengths range (150-2500nm), supplied by SHIMATZU (Japan). Liquid and solid (disk, and thin film) samples can be used with this instrument by changing the sample chamber for each case.

The fluorescence spectra were obtained using two instruments. The first one was constructed with wavelength range of 185-630 nm. Laser-induced fluorescence spectra of the dyes were measured using 405nm, 50mW, CW laser diode as excitation sources (other light sources could also be used). The second instrument was Quanta Master™ 40 Steady State Spectrofluorometer. The emission wavelength range of this instrument is 180-900 nm using CW xenon arc lamp as the excitation source with adjustable slits.

The PTI (Photon Technology international) lifetime instrument was used to measure the fluorescence lifetime for the prepared samples. This instrument includes nanosecond pulsed LED excitation sources in different ranges from 300 to 700 nm, and fast photomultiplier (PMT) in the spectral range 185-900 nm as a detector.

3. Results and Discussion

The energy transfer measurements of ACF dye (as donor) and RhB dye (as acceptor) in liquid and solid phases are presented using 405 nm as excitation wavelength. Two different type of solvent used, ethanol and DMSO as a proton transfer and non-proton transfer solvent, respectively. The study includes the absorption spectra, fluorescence spectra, fluorescence lifetime decay curves in each solvents.

The absorption spectra of mixture of ACF and RhB dyes dissolved in ethanol and DMSO are illustrated figures (2) and (3), respectively.

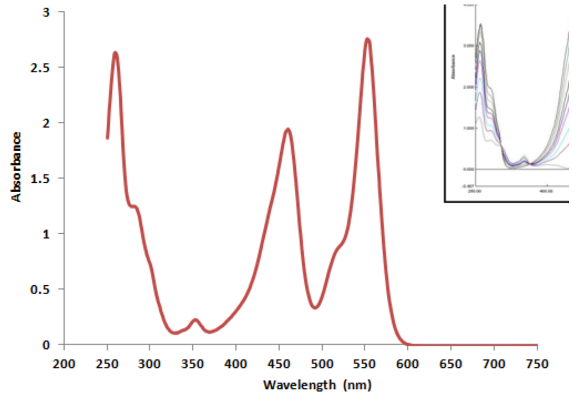

Fig. (2) Absorption spectrum for the mixture of 5×10^{-4}M ACF and 1×10^{-4}M RhB dyes in ethanol. Inset for 5×10-4M ACF with different concentrations of RhB dye

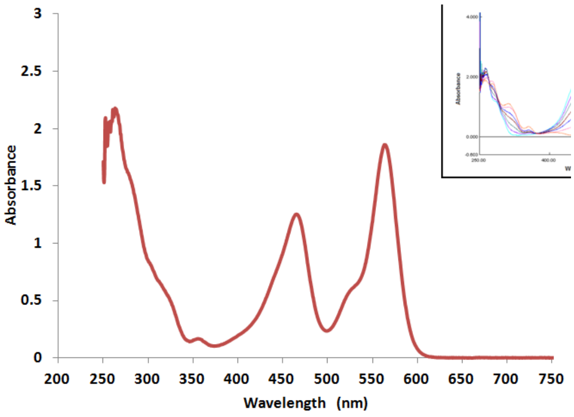

Fig. (3) Absorption spectrum for the mixture of 5×10^{-5}M ACF and 1×10^{-4}M RhB dyes in ethanol. Inset for 5×10^{-5}M ACF with different concentrations of RhB dye

The fluorescence spectra for the ACF+RhB mixture dissolved in ethanol and DMSO were recorded using PTI QM40 instrument taking 405 nm as the excitation wavelength. This wavelength was chosen because the absorption of RhB is negligible at this wavelength. For the energy transfer mechanism, the donor (ACF dye) concentration was fixed at 5×10^{-4} M as it was one of the most efficient concentration in ethanol mixed with different concentrations of the acceptor (RhB dye) in the range of 1×10^{-3} to 1×10^{-6} M. While the ACF concentration was fixed at 5×10^{-5} M in DMSO with different concentrations of RhB dye in the range of 1×10^{-3} to 1×10^{-5} M. Figures (4) and (5) show the fluorescence spectra for the mixtures in ethanol and in DMSO, respectively.

As one can see from figures (4) and (5) that the fluorescence intensity of ACF decreases as the concentration of RhB increases, while that of RhB increases. This is because of the energy transfer from ACF to RhB.

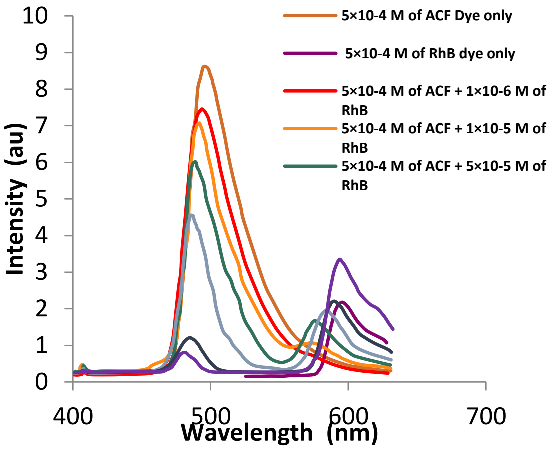

Fig. (4) Fluorescence spectra of ACF+RhB in ethanol for 5×10^{-4} M of ACF with different concentrations of RhB

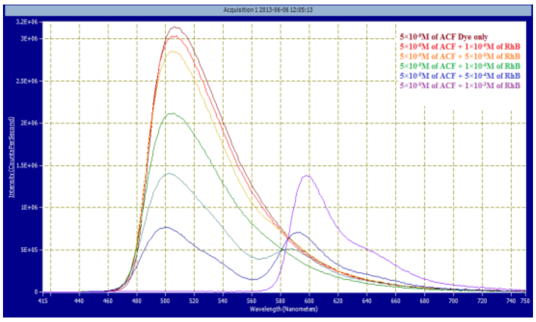

Fig. (5) Fluorescence spectrum of ACF+RhB in DMSO for 5×10^{-5}M of ACF with different concentrations of RhB

The parameters of fluorescence energy transfer that can be calculated from the fluorescence spectrum of the mixture of two dyes includes Stern-Volmer constant K_{SV}, half-value concentration $[A]_h$, efficiency of energy transfer F_{AD}, critical transfer distance R_o, and energy transfer rate parameter K_{AD}.

The parameters of above energy transfer between donor and acceptor for the mixture of ACF and RhB dyes were determined by measuring the quenching of donor fluorescence, or reduction of fluorescence lifetime. The former was applied in the present work. Since the fluorescence quantum yield of donor ϕ_{AD} is proportional to the peak of fluorescence intensity I, from the Stern-Volmer relation for energy transfer, we have

$$\frac{I_0}{I} = 1 + K_{SV}[A] \qquad (10)$$

where I_0 and I are the peak fluorescence intensities of donor without and with acceptor, respectively

Figure (6) shows the Stern-Volmer plot of I_0/I versus the acceptor (RhB) concentration [A], for ACF-RhB mixtures in ethanol and DMSO.

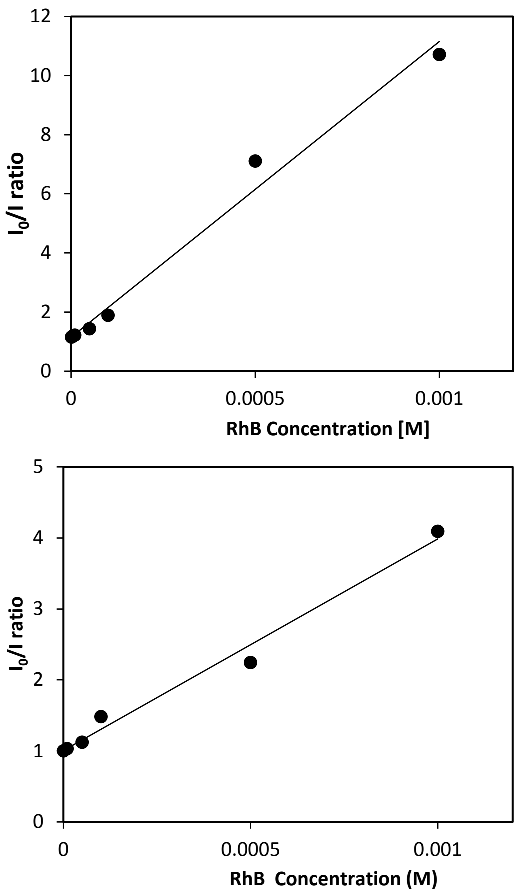

Fig. (6) The I_o/I ratio of ACF+RhB dye mixture as a function of the concentration of RhB dye in 5x10^{-4} M ethanol (upper), and in 5x10^{-4} M DMSO (lower)

Hence, the values of Stern-Volmer constant K_{SV} were calculated from the slope of best fit straight lines in Fig. (6). These values are listed in table (1). The values of $[A]_h$, R_o, F_{AD}, and K_{AD} [calculated from Eqs. (4)–(7)] are listed in table (1) too.

The energy transfer rate parameter K_{AD} was calculated from Eq. (6), using the measured values τ_D, which is the lifetime of the donor (ACF) alone without the acceptor (RhB). The lifetime values for 5×10^{-4} M of ACF were measured using PTI life instrument to obtain τ_D= 4.279 ns, giving K_{AD}= 2.115×10^{12} $M^{-1}s^{-1}$ in ethanol, and τ_D= 2.753 ns giving K_{AD}= 1.0825×10^{12} $M^{-1}s^{-1}$ in DOMS.

The total energy transfer efficiencies (F_{AD}) for the two solutions of ACF+RhB system were calculated at different concentrations. The plots are as shown in Fig. (7). The shape of these plots is exponential in nature and the values in the former case (ACF+RhB in ethanol) are at little higher side as compared to the latter one in DMSO. Theoretical calculations and the results from these considerations indicate that:

(i) At very low concentration range, [A] $<2\times10^{-4}$ M, the radiative transfer is the dominant mechanism. At these concentrations, simultaneous photon emissions at two separate spectral regions are expected.

(ii) In the range of concentration in which photon emissions is possible only in acceptor band spectrum, [A] $>2\times10^{-4}$ M, these relation show that both radiative and non-radiative energy transfer mechanism play important role in both cases.

Table (1) Parameters of fluorescence energy transfer for ACF-RhB mixtures in ethanol and DMSO

Acriflavine dye concentration					
5×10^{-4} M in ethanol			5×10^{-5} M in DMSO		
K_{SV} (M^{-1})	$[A]_h$ (M)	R_o (Å)	K_{SV} (M^{-1})	$[A]_h$ (M)	R_o (Å)
10.006×10^{3}	9.99×10^{-5}	158.405	2.980×10^{3}	3.3×10^{-4}	106.361
[RhB] (M)	F_{AD} in ethanol		[RhB] (M)		F_{AD} in DMSO
1×10^{-6}	0.0099		1×10^{-5}		0.02894
5×10^{-6}	0.0476		5×10^{-5}		0.1297
1×10^{-5}	0.0909		1×10^{-4}		0.2296
5×10^{-5}	0.333		5×10^{-4}		0.5984
1×10^{-4}	0.5		1×10^{-3}		0.7487
5×10^{-4}	0.8334		----		----
1×10^{-3}	0.909		----		----
$\tau_{D\ of}$ ACF only ns	K_{AD} in ethanol $M^{-1}s^{-1}$		$\tau_{D\ of}$ ACF only ns		K_{AD} in DMSO $M^{-1}s^{-1}$
4. 279	2.115×10^{12}		2.753		1.0825×10^{12}

The critical transfer distance R_0 corresponds to an average distance of the acceptor molecule in a sphere with radius R_0 having the excited donor molecule at the center. The values of R_0 are larger as compared to that of collisional transfer (the R_0 values for collisional transfer are reported to be in the range of 1–10Å [13]), especially in ethanol solution is larger as compared to that of DMSO solution. So to avoid the Dexter-type transfer, the distance between donor and acceptor should be >10Å.

Furthermore, the values of K_{AD} in the present work [~ 10^{12} $M^{-1}s^{-1}$] are much larger as compared to that of radiative energy transfer [~10^{9} $M^{-1}s^{-1}$] or to collisional transfer K_{diff} [~10^{9}-10^{10} $M^{-1}s^{-1}$], where for example K_{diff} is given by

$$K_{diff.} = 8\,RT/3000\,\eta \qquad (11)$$

where R is the gas constant, T is the temperature of the solution, and η is its viscosity. For example K_{diff}= 5.4x10^{9} $M^{-1}s^{-1}$ for ethanol solution at room temperature [14]

This indicates that the resonance energy transfer is the dominant mechanism for energy transfer.

The achieved results from figures (6) and (7), and table (1) indicate that the energy transfer efficiency increases with increase of the acceptor (RhB) concentration at a fixed donor (ACF) concentration, and approaches unity at high concentration, leading to leveling off the energy transfer mechanism or in other words it becomes the dominant mechanism. This is in agreement with the obtained results of other donor acceptor pairs [13,15].

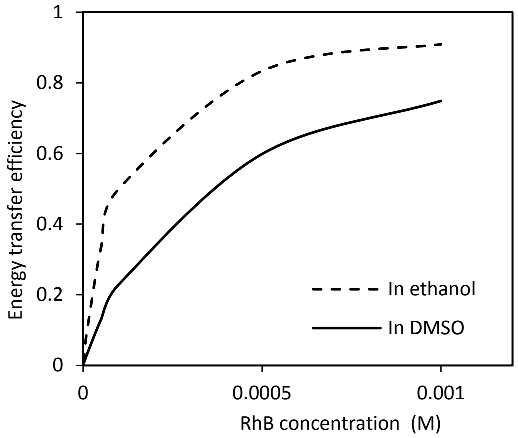

Fig. (7) Energy transfer efficiency of ACF+RhB mixture as a function of RhB concentration in ethanol and DMSO

The energy transfer represent one of the parameters used to reduce the photobleaching of acceptor dye, as it is known by increasing the bleaching time, the magnitude of absorption features in the visible region of the spectrum decreases and the rate of decreases is depend on the wavelength of bleaching, shorter wavelengths leading to increase the bleaching rate [16,17]. So according to this, one of the important parameters that used to decrease the influence of photobleaching via energy transfer by use the mixture of two dyes as a donor and acceptor.

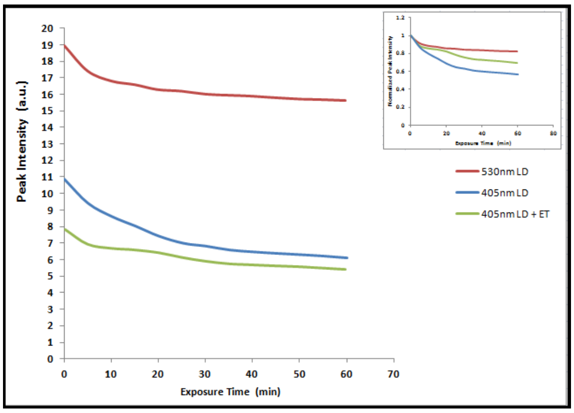

Fig. (8) Peak fluorescence intensity vs. time of exposure for disks of RhB and ACF+RhB mixture using 405nm and 530nm LDs. Inset is the normalized decay

The energy emitted by ACF dye only is absorbed by the RhB dye to get their characteristic emission. In this mechanism the RhB dye excited by longer wavelength than that 405 nm LD leading to decrease of bleaching rate. The continuous exposure for the disk sample of RhB dye doped PMMA to each of 405 nm and 530 nm LDs of 1mW output power for one hour and record the decay curve for each case and by record the decay curve for a disk sample combine of ACF and RhB dyes for 405nm LD, as shown in Fig. (8). The achieved result gives an indication of the energy transfer reduce the bleaching rate of RhB dye from 43.8 to 30.6%. The acceptor photobleaching technique can be employed to measuring FRET in different fields for example in biomedical field with cell surface protein label; it depends on the increase in donor fluorescence after complete acceptor photobleaching represent a measured of the FRET efficiency.

4. Conclusions

In concluding remarks, the fluorescence spectra of a mixture of two laser dyes; acriflavine and rhodamine B in different solvents; ethanol and DMSO, were recorded and studied. The energy transfer efficiency of the prepared samples was determined and studied by comparing some parameters such as the critical transfer distance, the emission lifetime, and the rate constant for energy transfer at different concentrations of these solutions. The emission lifetime of the dye mixture in DMSO was shorter than that in ethanol by 35.6%.

References

[1] H. Stegemeyer, **“Book Review: Photoluminescence of Solutions. By C. A. Parker”**, Angewandte Chemie International Edition in English, 8(12),1969.

[2] R. Ghazy et al., “Experimental Investigations on Energy-Transfer Characteristics and Performance of Some Laser Dye Mixtures”, Opt. Laser Technol., 34(2) (2002).

[3] M. Isaksson et al., “On the Quantitative Molecular Analysis of Electronic Energy Transfer within Donor-Acceptor Pairs”, Phys. Chem. Chem. Phys., 9(16) (2007).

[4] M.F.a.K. Mito, “Solid-State Dye Laser with Photo-Induced Distributed Feedback”, Jpn J. Appl. Phys., 39(10) Pt 1 ((2000) 5859.

[5] J.B. Birks, **“Photophysics of Aromatic Molecules”**, Wiesly Interscience (London, 1973).

[6] J.A. Barltrop and J.D. Coyle, “Excited States in Organic Chemistry”, John-Wiley & Sons (London, 1975).

[7] T. Mitsugu and O. Yujiro, “Energy Transfer Mechanism and Amplified Spontaneous Emission Characteristics of Dye Mixture Solutions”, Jpn J. Appl. Phys., 22(9) (1983) 1392.

[8] R.D. Singh et al., “Time-Resolved Spectra of Coumarin 30-Rhodamine 6g Dye Mixture”, Pramana – J. Phys., 34(1) (1990).

[9] A.R.N. Sesha Bamini and V.S. Gowri, “Effect of Different Donors and a Polymer Environment on Photophysical and Energy Transfer Studies Using C540 as the Acceptor”, Pramana – J. Phys., 79(6) (2012) 1503.

[10] E.M. Graham, “The Application of Fluorescence Lifetime Imaging Microscopy to Quantitatively Map Mixing and Temperature in Microfluidic Systems”, PhD thesis, University of Edinburgh, 2007.

[11] P.I.H. Bastiaens and T.M. Jovin, **“Fluorescence Resonance Energy Transfer (Fret)**

Microscopy in Cell Biology”. 2nd ed., Academic Press (NY, 1998).

[12] S.R. Bobbara, “Energy Transfer between Molecules in the Vicinity of Metal Nanoparticle”, MSc thesis, Queen's University, 2011.

[13] Z.F.M. Al-Bawi, MSc thesis, University of Technology, 1997.

[14] Z.S. Sadik, “Thin Film Energy Transfer Dye Laser”, PhD thesis, Baghdad University, 2002.

[15] C. Vijila and A. Ramalingam, “Photophysical Characteristics of Coumarin 485 Dye Doped Poly(Methyl Methacrylate) Modified with Various Additives”, J. Mater. Chem., 11(3) (2001).

[16] Ed. McKenna et al., “Kinetic Model of Irreversible Photobleaching of Dye-Doped Polymer Waveguide Materials”, J. Opt. Soc. Am. B, 21(7) (2004) 1294.

[17] D. Tomic and A.R. Mickelson, “Photobleaching for Waveguide Formation in a Guest-Host Polyimide”, Appl. Opt., 38 (1999) 3893.

IRAQI JOURNAL OF APPLIED PHYSICS
Vol. 16, No. 3, July-September 2020, pp. 39-42

Reem H. Turki
Mohammed A. Hameed

Department of Physics,
College of Science,
University of Baghdad,
Baghdad, IRAQ

Spectral and Electrical Characteristics of Nanostructured NiO/TiO_2 Heterojunction Fabricated by DC Reactive Magnetron Sputtering

In this work, p-n junctions were fabricated from highly-pure nanostructured NiO and TiO_2 thin films deposited on glass substrates by dc reactive magnetron sputtering technique. The structural characterization showed that the prepared multilayer NiO/TiO_2 thin film structures were highly pure as no traces for other compounds than NiO and TiO_2 were observed. It was found that the absorption of NiO-on-TiO_2 structure is higher than that of the TiO_2-on-NiO. Also, the NiO/TiO_2 heterojunctions exhibit typical electrical characteristics, higher ideality factor and better spectral responsivity when compared to those fabricated from the same materials by the same technique and with larger particle size and lower structural purity.

Keywords: Multilayer structure; Magnetron sputtering; Nanostructures; Metal oxides
Received: 18 August 2020; **Revised:** 6 September 2020; **Accepted:**13 September 2020

1. Introduction

For more than six decades, semiconductor heterojunctions attract the research interest due to their effectiveness in photonics and optoelectronics applications, especially solar cells, photodetectors and gas sensors. With a wide range of semiconductors and variety of their properties, heterojunctions can cover wide range of uses. As well, the transfer from micro to nanoscale structures allowed to discover new uses of heterojunctions with relatively different characteristics [1-3].

The formation of a heterojunction from two different semiconducting materials allows to invest the properties of both materials to serve some important practical applications in addition to new possible properties of the junction to serve new applications [4,5].

The structural purity of the semiconducting materials forming the heterojunction plays a key role in its performance as no contributions are expected due to the existence of impurities or other compounds within the crystalline structures of both materials [6]. Synthesis of highly-pure semiconductors is one of the most requiring processes to take care of preparation conditions and parameters. Among many methods and techniques used to synthesize semiconductors, plasma sputtering is one of the most important due to its low cost, open technology, reliability and good control of preparation parameters to ensure the production of highly-pure structures [7,8]. Also, this technique allows to produce nanostructures from semiconducting materials with high structural purity and distinguished specifications [9].

Nickel oxide (NiO) and titanium dioxide (TiO_2) are categorized as wide semiconductors (3.2 and 3.85 eV, respectively) and excellent candidates for many applications of semiconductors. TiO_2 is an important semiconductor for photocatalysis and the first candidate to fabricate efficient photocatalyst devices [10,11]. As well, NiO is an excellent candidate to fabricate gas sensors, dye sensitized photocathodes, electrodes in alkaline batteries, resistive switching, and electrochromic smart windows [12-14]. The energy outline of the heterojunction made from NiO and TiO_2 can be shown in Fig. (1).

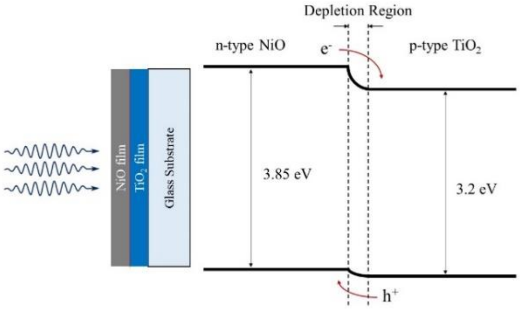

Fig. (1) Energy outline of the nanostructured NiO/TiO_2 heterostructure

The small difference between valence and conduction bands in both materials makes it easy for charge carriers to transfer from one side of the heterojunction to the other. The depletion region formed at the junction may exhibit new characteristics while both sides keep their original properties [15].

In this work, p-n heterojunctions were fabricated from highly-pure nanostructures of NiO and TiO_2 by dc reactive magnetron sputtering technique and their spectroscopic and optoelectronic characteristics were determined.

2. Experimental Part

A home-made dc reactive magnetron sputtering system was used in this work. Two highly-pure Ti and Ni targets (99.99%) were sputtered in presence of oxygen to deposit TiO_2 and NiO thin films on glass substrates. The deposition chamber was initially evacuated down to 0.001 mbar and then filled with gas mixture of argon and oxygen with mixing ratio of 1:1. The pressure of gas mixture was about 0.8 mbar and the discharge current was 20 mA. More details on the sputtering system and its operation parameters can be found elsewhere [16-21]. The optimized conditions to prepare nanostructures from both materials were presented in previous studies on the same system [22-24].

The deposited thin films were extracted as powders by a novel technique known as conjunctional freezing-assisted ultrasonic extraction method [7,8].

The two possible configurations of the multilayer structure (NiO-on-TiO_2 and TiO_2-on-NiO) were compared and the results showed that the first configuration exhibits higher absorbance than the second one. Therefore, all results were presented for the first configuration shown in Fig. (2).

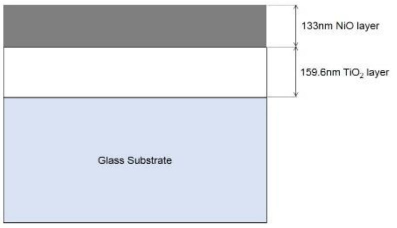

Fig. (2) The configuration of multilayer NiO/TiO_2 thin film structure prepared in this work

The spectroscopic characteristics were determined by a KMAC S2100 UV-visible spectrophotometer in the spectral range of 200-900 nm with a resolution of 0.2 nm. The optoelectronic characteristics were determined by using a dc voltage supply (DHF-1502DD) and a Keithley480 picoammeter. The light characteristics were measured by illuminating the fabricated device with a 10 mW light source. The structural characteristics were determined by the x-ray diffraction (XRD) patterns recorded using a Philips PW1730 diffractometer with Cu source (λ=1.54060Å).

3. Results and Discussion

Figure (3) shows the XRD pattern of the multilayer structure fabricated from the NiO thin film deposited on the TiO_2 thin film deposited on glass substrate. The film thickness of NiO and TiO_2 films was 133 and 159.6 nm, respectively. Referring to the JCPDS cards [25] of both NiO and TiO_2, all peaks observed in this pattern are belonging to NiO and TiO_2 compounds only without any peak belonging to the free metal (Ni or Ti) neither to other compounds. This initially highlights the structural purity of the prepared multilayer structure.

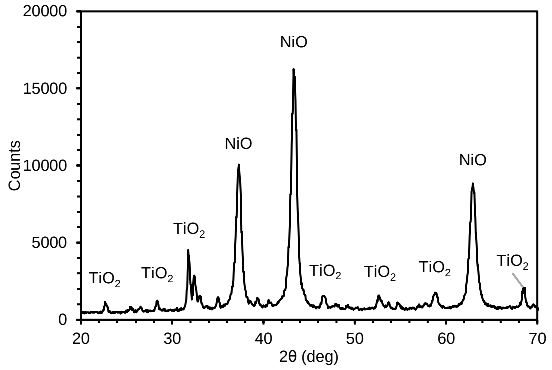

Fig. (3) XRD pattern of multilayer NiO/TiO_2 structure prepared in this work

To confirm the formation of the required compounds (NiO and TiO_2) as well as the structural purity of the prepared samples, the FTIR spectra were recorded for each sample individually, in the spectral range of 400-4000 cm^{-1}, as shown in Fig. (4). The band assigned at 1064 cm^{-1} is ascribed to the vibration of the Ni-O bond [26] while three bands are observed for the TiO_2 sample at 409, 447 and 667 cm^{-1}, which ascribed to the vibration modes of the triatomic molecule (TiO_2) [26]. No bands ascribed to compounds other than O-H were observed, which confirms the structural purity of both types of samples (NiO and TiO_2). However, the O-H bands are unavoidable due to the adsorption of water from the environment.

Figure (5) shows the absorption spectra of the NiO/TiO_2 heterojunction fabricated in this work as compared to the summation of absorbance of both materials when deposited individually. The difference reaches its maximum of about 850% at 461 nm. It is clear that the increase in absorbance is attributed to the formation of the heterojunction and its characteristics. Also, the heterojunction structure shows high absorption in the UV region and an absorption edge at about 490 nm is observed while both materials show such high absorption at wavelengths shorter than 440 nm. This red shift in absorption spectrum can be invested for better absorption of the visible radiation and hence using this heterojunction in the fabrication of photodetectors and solar cells.

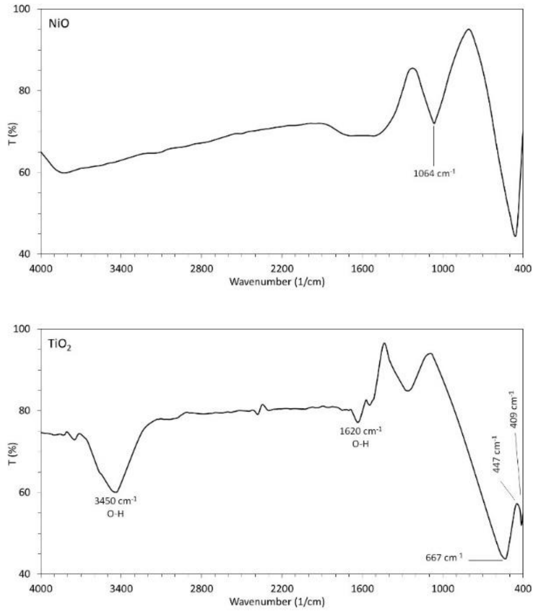

Fig. (4) FTIR spectra of NiO and TiO_2 samples prepared in this work

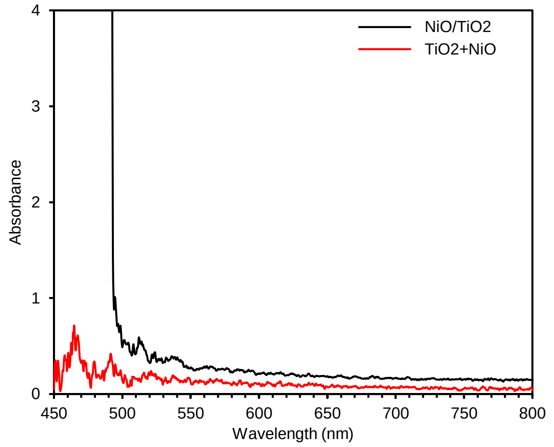

Fig. (5) Absorption spectra of nanostructured NiO/TiO_2 heterostructure fabricated in this work

Figure (6) shows the I-V characteristics in dark and under 10mW illumination for the NiO/TiO_2 heterojunction fabricated in this work. As shown, typical behavior is observed as the dark current is about 3.5μA while the photocurrent reaches a maximum at about 107μA. Accordingly, the ideality factor of this heterojunction can be determined to be 3.02.

Figure (7) shows the spectral responsivity of the nanostructured NiO/TiO_2 heterostructure fabricated in this work. The heterostructure shows relatively low responsivity (<0.3) to the wavelengths shorter than 300 nm (UV). Similarly, this heterostructure shows low responsivity (<0.4) to the wavelengths longer than 800 nm (NIR). The responsivity of this heterostructure exceeds 0.6 for the wavelengths in the visible region (400-700 nm). Therefore, this heterojunction device can be successfully used to fabricate photonic and optoelectronic devices like photodetectors and solar absorbers with relatively better characteristics than those of the thin film NiO/TiO_2 heterojunction with larger particle size.

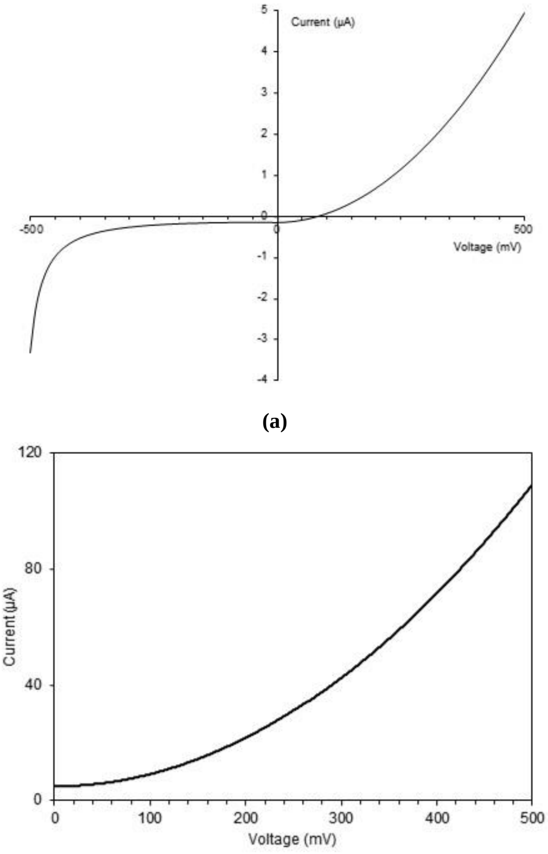

(a)

(b)

Fig. (6) The I-V characteristics in dark (a) and under 10mW illumination (b) for the NiO/TiO_2 heterojunction fabricated in this work

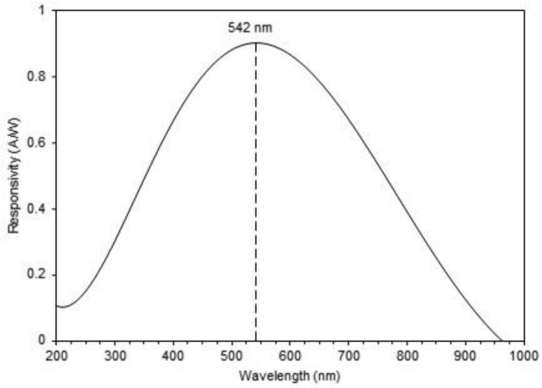

Fig. (7) Spectral responsivity of the nanostructured NiO/TiO_2 heterostructure fabricated in this work

4. Conclusions

In concluding remarks, an efficient p-n heterojunction was fabricated from NiO and TiO_2 nanostructures synthesized by dc reactive magnetron sputtering technique. This heterojunction shows better spectroscopic and electrical characteristics than the similar structures fabricated from the same materials (NiO and TiO_2) of larger particle size. The photocurrent obtained at the same levels of applied voltage is relatively lower, however, the ideality factor is reasonably higher. The spectral responsivity of this heterojunction in the visible region encourages to use it in the fabrication of nanostructured thin film optoelectronics such as photodetectors and solar cells.

References

[1] W.A. Goddard et al., **"Handbook of Nanoscience, Engineering and Tehnology"**, CRC Press (FL, 2003), p. 65

[2] B. Bhushan, **"Springer Handbook of Nanotechnology"**, Springer-Verlag (Berlin, 2004), p. 1.

[3] B.S.R. Reddy, **"Advances in Diverse Industrial Applications of Nanocomposites"**, InTech (2011), p. 57.

[4] M. Ohring, **"The Materials Science of Thin Films"**, Academic Press (London, 1992), p. 310.

[5] E. Kaxiras, **"Atomic and Electronic Structure of Solids"**, Cambridge University Press (NY, 2003), p. 342.

[6] J. Cheng et al., "Recent Advances in Optoelectronic Devices Based on 2D Materials and Their Heterostructures", Adv. Opt. Mater., 7(1) (2019) 1800441.

[7] O.A. Hammadi, "Production of Nanopowders from Physical Vapor Deposited Films on Nonmetallic Substrates by Conjunctional Freezing-Assisted Ultrasonic Extraction Method", Proc. IMechE, Part N, J. Nanomater. Nanoeng. Nanosys., 232(4) (2018) 135-140.

[8] O.A. Hammadi, "Effects of Extraction Parameters on Particle Size of Titanium Dioxide Nanopowders Prepared by Physical Vapor Deposition Technique", Plasmonics, 15 (2020) doi: 10.1007/s11468-020-01205-8

[9] J. Jeevanandam et al., "Review on nanoparticles and nanostructured materials: history, sources, toxicity and regulations", Beilstein J. Nanotech., 9 (2018) 1050-1074.

[10] D.P. Woodruff, "The Chemical Physics of Solid Surfaces", vol. 12, Elsevier (Amsterdam, 2007), p. 237.

[11] A. Zaleska, "Doped-TiO_2: A Review", Recent Patents on Eng., 2 (2008) 157-164.

[12] S. Shen et al., "Titanium dioxide nanostructures for photoelectrochemical applications", Prog. in Mater. Sci., 98 (2018) 299-385.

[13] D. Ziental et al., "Titanium Dioxide Nanoparticles: Prospects and Applications in Medicine", Nanomater., 10 (2020) 387-31.

[14] F.I. Ezema A.B.C Ekwealor and R.U. Osuji, "Optical properties of chemical bath deposited nickel oxide (NiO_x) thin films", Superficies y Vacío, 21(1) (2008) 6-10.

[15] R. Frisenda et al., "Atomically thin p–n junctions based on two-dimensional materials", Chem. Soc. Rev., 47(9) (2018) 3339-3358.

[16] O.A. Hammadi et al., "Operation Characteristics of a Closed-Field Unbalanced Dual-Magnetrons Plasma Sputtering System", Bulg. J. Phys., 41(1) (2014) 24-33.

[17] F.J. Kadhim and A.A. Anber, "Microhardness of Nanostructured Si_xN_{1-x} Thin Films Prepared by Reactive Magnetron Sputtering", Iraqi J. Appl. Phys., 12(2) (2016) 15-19.

[18] O.A. Hammadi, M.K. Khalaf, F.J. Kadhim, "Fabrication and Characterization of UV Photodetectors Based on Silicon Nitride Nanostructures Prepared by Magnetron Sputtering", Proc. IMechE, Part N, J. Nanoeng. Nanosys., 230(1) (2016) 32-36.

[19] O.A. Hammadi, M.K. Khalaf, F.J. Kadhim, "Silicon Nitride Nanostructures Prepared by Reactive Sputtering Using Closed-Field Unbalanced Dual Magnetrons", Proc. IMechE, Part L, J. Mater.: Design and Applications, 231(5) (2017) 479-487.

[20] M.A. Hameed and Z.M. Jabbar, "Optimization of Preparation Conditions to Control Structural Characteristics of Silicon Dioxide Nanostructures Prepared by Magnetron Plasma Sputtering", Silicon, 10(4) (2018) 1411-1418.

[21] O.A. Hammadi and N.E. Naji, "Characterization of Polycrystalline Nickel Cobaltite Nanostructures Prepared by DC Plasma Magnetron Co-Sputtering for Gas Sensing Applications", Photon. Sens., 8(1) (2018) 43-47.

[22] O.A. Hammadi, M.K. Khalaf, F.J. Kadhim, "Fabrication of UV Photodetector from Nickel Oxide Nanoparticles Deposited on Silicon Substrate by Closed-Field Unbalanced Dual Magnetron Sputtering Techniques", Opt. Quantum Electron., 47(12) (2015) 3805-3813.

[23] E.A. Al-Oubidy and F.J. Al-Maliki, "Effect of Gas Mixing Ratio on Energy Band Gap of Mixed-Phase Titanium Dioxide Nanostructures Prepared by Reactive Magnetron Sputtering Technique", Iraqi J. Appl. Phys., 14(4) (2018) 19-23.

[24] F.J. Al-Maliki and E.A. Al-Oubidy, "Effect of gas mixing ratio on structural characteristics of titanium dioxide nanostructures synthesized by DC reactive magnetron sputtering", Physica B: Cond. Matter, 555 (2019) 18–20.

[25] Standard X-Ray Diffraction Powder Patterns, Section 11, p. 47, Section 7m, pp. 82-83National Bureau of Standards, Monograph 25 (1980).

[26] N.N. Greenwood and E.J.F. Ross, **"Index of Vibrational Spectra of Inorganic and Organometallic Compounds"** vol. III, Butterworth Group (London, 1966), p. 800, 1078.

**THE IRAQI JOURNAL OF
APPLIED PHYSICS**
EDITORIAL BOARD

COPYRIGHT RELEASE FORM
IRAQI JOURNAL OF APPLIED PHYSICS (IJAP)

We, the undersigned, the author/authors of the article titled
………
………
………
………
………
………
………

that is submitted to the Iraqi Journal of Applied Physics (IJAP) for publication, declare that we have neither taken part or full text from any published work by others, nor presented or published it elsewhere in any other journal. We also declare transferring copyrights and conduct of this article to the Iraqi Journal of Applied Physics (IJAP) after accepting it for publication.

The authors will keep the following rights:
1. Possession of the article such as patent rights.
2. Free of charge use of the article or part of it in any future work by the authors such as books and lecture notes after informing IJAP editorial board.
3. Republishing the article for any personal purposes of the authors after taking journal permission.

To be signed by all authors:

Signature:…………………………………………………………..date: …………………………………………
Printed name: ………………………………………………………………………………………………………

Signature:…………………………………………………………..date: …………………………………………
Printed name: ………………………………………………………………………………………………………

Signature:…………………………………………………………..date: …………………………………………
Printed name: ………………………………………………………………………………………………………

Correspondence
address:…………………………………………………………………………………………………..
……
Address:……………………………………………………………………………………………………
……
Telephone:…………………………..…………………..email: ………………………………………………………

Note: Complete and sign this form and mail it to the below address with your finally revised manuscript

The Iraqi Journal of Applied Physics
www.iraqiphysicsjournal.com
Email: info@iraqiphysicsjournal.com
Email: editor_ijap@yahoo.co.uk
Email: irq_appl_phys@yahoo.com

IRAQI JOURNAL OF APPLIED PHYSICS

Volume (16), Issue (3), July-September 2020

CONTENTS